Silicon Electrolyte Interface Stabilization (SEISta)
Quarter 3 FY19

Anthony Burrell

National Renewable Energy Laboratory
15013 Denver West Parkway
Golden, CO 80401
Phone: (303) 384-6666
E-mail: anthony.burrell@nrel.gov

Brian Cunningham, DOE-EERE-VTO Program Manager

Hybrid Electric Systems, Battery R&D
Phone: (202) 586-8055
E-mail: brian.cunningham@ee.doe.gov

Table of Contents

Project Introduction

This report documents the Silicon Electrolyte Interface Stabilization team's approach in 1) characterizing the early-stage silicon-electrolyte interphase (SEI) including progress on identifying the specific reaction pathways present in the formation of the SEI layer, and 2) establishing a procedure for measuring SEI growth rate at fixed potentials and different cycling regimes.

Silicon is a viable alternative to graphitic carbon as an electrode in lithium-ion cells and can theoretically store >3,500 mAh/g. However, lifetime problems have been observed that severely limit its use in practical systems. The major issues appear to involve the stability of the electrolyte and the uncertainty associated with the formation of a stable SEI at the electrode. Recently, calendar-life studies have indicated that the SEI may not be stable even under conditions where the cell is supposedly static. Clearly, a more foundational understanding of the nature of the silicon/electrolyte interface is required if we are to solve these complex stability issues. A new multi-lab consortium has been formed to address a critical barrier in implementing a new class of materials used in lithium-ion batteries that will allow for smaller, cheaper, and better-performing batteries for electric-drive vehicles. This consortium, named the Silicon Electrolyte Interface Stabilization (SEISta) project, was formed to focus on overcoming the barrier to using such anode materials. Five national laboratories are involved: the National Renewable Energy Laboratory (NREL), Argonne National Laboratory (ANL), Lawrence Berkeley National Laboratory (LBNL), Oak Ridge National Laboratory (ORNL), and Sandia National Laboratories (SNL).

The SEISta project was specifically developed to tackle the foundational understanding of the formation and evolution of the solid-electrolyte interphase on silicon. This project will have as its primary goal an understanding of the reactivity of the silicon and lithiated silicon interface with the electrolyte in lithium-ion systems. It consists of researchers from multiple national laboratories (NREL, ANL, LBNL, ORNL, and SNL) working toward clear unified goals. The Silicon Deep-Dive team, which focuses on the science and technology

barriers in functional electrodes, is a critical partner in this work. Many of the researchers are shared between both teams, and we hold joint meetings to ensure effective communication between the teams.

The current goals of SEISta are:

Quarter 1 Milestone: Have determined if the pristine surface of the silicon influences the composition and the function of the SEI after 1, 10, and 50 cycles (XPS, SIMS, IR, and Raman, STEM, SSRM). (100% complete)

Quarter 2 Milestone: Have determined that the nature of the silicon surface can affect the composition, function, and thickness of the SEI. (100% complete)

Quarter 3 Milestone: Have determined how water concentration (as a function of water content up to 100 ppm) in the electrolyte affects SEI thickness and composition (electrochemistry, spectroscopy, impedance) of the SEI formed at 1.5, 1.0, 0.7, 0.4, 0.15, and 0.05 V vs Li/Li+. (100 % complete)

Quarter 4 Milestone: Have determined the nature of the soluble SEI components that are formed over 10 cycles and that are soluble in the Gen 2 electrolyte.

Approach

The SEISta team works to ensure that protocols for sample preparation, experimental design, and implementation as well as data reporting are consistent across the whole team. Each laboratory is working toward the same set of quarterly milestones using its own specific talents and capabilities in a concerted effort with the other team members. This joint focus results in multiple researchers interacting to produce and analyze data to ensure that individual experimental variations will not lead to erroneous results. Critical to the success of this effort is the use of standard samples that can be shared by all parties. In addition to weekly whole-team video presentations, we have held on-site face-to-face meetings each quarter for all team members and other interested parties to brainstorm and sort out issues with existing experiments and jointly develop new experimental plans.

Objectives

The critical issues that SEISta is attempting to address are:

- What are the properties of the lithiated silicon/electrolyte interface?

- What is the silicon SEI actually made of and what reactions are contributing to it?

- How fast does the silicon SEI grow?

- Does it stop growing?

- Is it soluble?

- Can it be stabilized?

For FY19, the team continues to focus on three broad tasks:

Materials Standardization – This task is critical to developing and deploying standardized samples and experimental procedures across the team. We will continue to provide full characterization to any new sample that is to be used for SEI studies to ensure reproducibility and full understanding of the material. This quarter's work focused on developing new oxide coatings and methods to control the thickness and density of oxide samples. In addition, work on the silicon nanoparticles has made progress with the enhancement of the materials collection and handling system in the plasma reactor. *Although this work dominated the early part of the project and is still critical to its success, it is now only a minor part of the work and this is reflected in the relative balance of this quarterly report.*

Model Materials Development and Characterization – The nature of the electrode-electrolyte interaction in silicon electrodes is at the heart of the formation and stability of the SEI. The inherent chemical reactivity of silicon with common electrolytes has been a focus for this team and will be a primary focus moving to quarter 2. The synthesis of well-defined silicon nanoparticles and the different chemical markups of lithiated silicon surfaces is being probed by preparing model compounds and thin films that may/can exist in silicon anodes. Lithium silicides, silicates, and other inorganic material (LiF, Li_2O) are being prepared, and their reactivity with electrolytes is being determined. These materials also act as standard spectroscopy samples for the researchers who are looking at the formation of the SEI on different silicon materials.

SEI Characterization – The overall objective for SEISta is to understand the nature and evolution of the SEI on silicon anodes. The materials standardization and model compounds will enable the researchers to systematically investigate the formation of the solid-electrode interphase using a wide variety of the spectroscopy techniques—from different optical, microscopy, and electrochemistry—to determine how the SEI forms based on the nature of the silicon surface, and how it evolves over time. This section of work will continue to grow in scope as we move beyond the sample-characterization phase of the project and toward understanding the nature and evolution of the SEI. *This part of the project now represents the bulk of the work and, as such, this quarterly report is largely reporting on work leading to this outcome.*

SEISta Milestones FY19 Silicon Electrolyte Interface Stabilization (SEISta)

SEISta Team

Background

The overall objective of the SEISta project is to better understand the formation and evolution of the solid-electrolyte interphase (SEI) on silicon anodes. Silicon is a viable alternative to graphitic carbon as an electrode in lithium-ion cells and can theoretically store >3,500 mAh/g. However, lifetime problems have been observed that severely limit its use in practical systems. The major issues appear to involve the stability of the electrolyte and the uncertainty associated with the formation of a stable SEI at the electrode. Recently, calendar-life studies have indicated that the SEI may not be stable even under conditions where the cell is supposedly static. Clearly, a more foundational understanding of the nature of the silicon/electrolyte interface is required if we are to solve these complex stability issues. A multi-lab consortium has been formed to address a critical barrier in implementing a new class of materials used in lithium-ion batteries that will allow for smaller, cheaper, and better-performing batteries for electric-drive vehicles. This consortium—the Silicon Electrolyte Interface Stabilization (SEISta) project—was formed to focus on overcoming the barrier to using such anode materials. Five national laboratories, led by the National Renewable Energy Laboratory (NREL), are involved: NREL, as well as Argonne (ANL), Lawrence Berkeley (LBNL), Oak Ridge (ORNL), and Sandia National Laboratories (SNL).

Quarter 3 Milestone:
Have determined how water concentration (as a function of water content up to 100 ppm) in the electrolyte affects SEI thickness and composition (electrochemistry, spectroscopy, impedance) of the SEI formed at 1.5, 1.0, 0.7, 0.4, 0.15, and 0.05 V vs Li/Li+. (100 % complete).

This millstone was completed using a number of spectroscopic techniques coupled with electrochemistry. Specifically wafer samples using native oxide and SiH terminated wafers were examine at the required voltages. It was observed that small amounts of current were present at 0.7 and 1.0V due to the initial SEI current observed at 1.5V. So in some experiment the 0.7 and 1.0V holds were skipped. Examples of the experimental procedures employed are:

SEIs were formed on Si wafer with an extended potential hold at 0.01, 0.2, 0.5 and 1.0 V. At each potential, two samples were prepared: one with standard Gen2 electrolyte and another with Gen2 electrolyte with 50 ppm H_2O contamination. After disassembly, samples were characterized with AFM and SSRM. SEI formed with and without water at 0.2 V was found to be thinner and less rough than SEI formed at 0.01 V, suggesting that lithiation of the Si is responsible for greater electrolyte decomposition and SEI formation. SEIs formed at 0.5 and 1.0 V were dramatically thicker and rougher. Differences between the water contaminated samples and the Gen2 control were minimal; SSRM resistivity vs. depth profiles showed equivalent depths and resistivities within the SEI structures. Samples were prepared again to validate the results, and the same trends were verified.

In many cases the custom three-electrode o-ring cell, we performed electrochemical behavior analysis experiments with and without 50 ppm of water at the current density of 30 μA/cm2. The cell was suffered from side reactions in the first couple of cycles with Gen2 + 50 ppmH2O electrolyte, but the Si wafer eventually started to be lithiated from 4th or 5th cycle, which may indicate the initial formation of thicker SiEI layer with water. In the case of dQ/dV plots derived from voltage profiles for the Gen2 + 50 ppmH2O electrolyte, we observed a number of reduction peaks at around 0.6 - 0.35 V for the 1st cycle possibly due to additional parasitic reactions (e.g., electrolyte decomposition) with water and formation of SiEI with different component(s). Another interesting feature is that the dQ/dV plot of the 10th cycle with Gen2 + 50 ppmH2O electrolyte almost resembles that of the 2nd cycle with Gen2 electrolyte. This indicates that the initially formed SiEI layers (with water) may be dissolved into the electrolyte and/or detached from Si wafer surface, and the subsequently formed SiEI layer may not be affected by the water that may be mostly consumed during the initial cycles.

Part 1. The SiO$_2$ Interface

SEISta (Analytical Microscopy and Imaging Group, NREL)

Caleb Stetson, Andrew Norman, Yanli Yin, Chun-Sheng Jiang, Nathan Neale, Mowafak Al-Jassim (NREL)

Introduction

In this quarter, solid-electrolyte interphase (SEI) formed on silicon anodes was investigated at later stages of cycling (700 cycles). These results were comparatively analyzed with respect to previous work at earlier stages of cycling (pristine, 1, 10, and 50 cycles). Novel lithium-ion battery systems, namely Zintl phase materials, were also investigated via scanning transmission electron microscopy (STEM) and atomic force microscopy (AFM).

Results

Samples representing two model systems (5-nm thermally grown SiO$_2$ on Si wafer and native SiO$_x$ on Si wafer) were cycled for hundreds of cycles to investigate the evolution of SEI into later stages of cycling. Two electrochemical protocols were employed; *early-stage* SEI was formed without true lithiation/delithiation of the Si by giving current until an upper cutoff potential of 115 mV was reached, followed by three hours of resting. The *alternative* electrochemical protocol included two hours of lithiation followed by delithiation until a potential of 1.5 V was reached. All samples were cycled with a fixed current density of 6.82 µA cm^{-2} and given a final lithiation hold at 115-mV potential for 10 minutes.
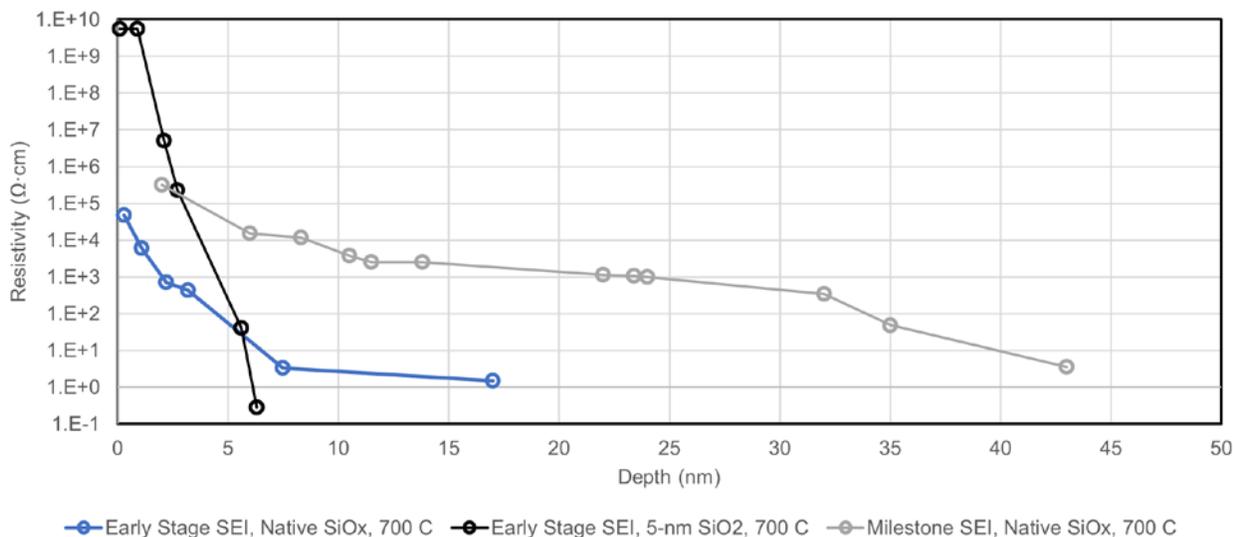
Figure 1. SSRM resistivity vs. depth profiles for SEIs at late stages of cycling.
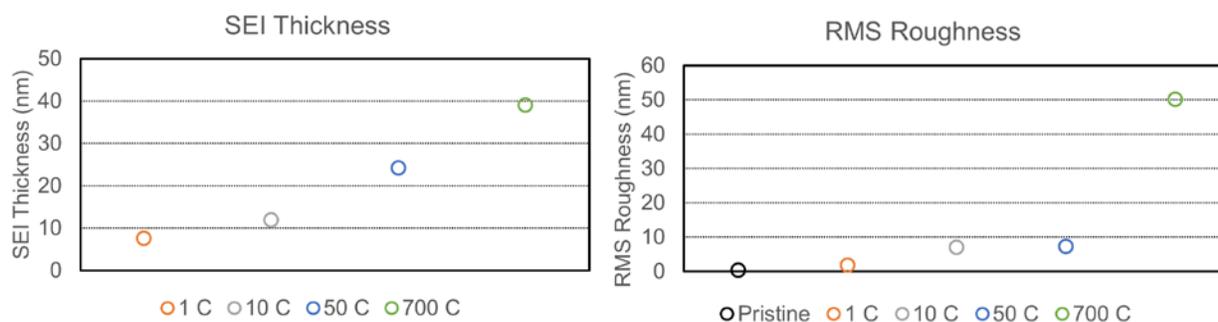
Figure 2. Results of SSRM resistivity vs. depth profiles for SEIs at late stages of cycling: SEI thickness and RMS roughness.

Results of resistivity vs. depth profiling (Fig. 1) indicate that the SEI thickness continues to grow into later stages of cycling at normal lithiation/delithiation conditions (Fig. 2). However, the growth rate attenuates significantly; the same increase in SEI thickness develops between 10 and 50 cycles as between 50 to 700 cycles. The development of AFM RMS roughness of SEI, however, differs significantly from this result: roughness increases dramatically after 700 cycles compared to the other points of cycling (Fig. 2). This result suggests that on a planar substrate, the SEI goes through various growth and dissolution processes under cycling that ultimately roughens the SEI that may, in part, contribute to its instability.

A composite Si electrode with a formed Zintl phase was examined by AFM and STEM after one full cycle. The electrolyte mixture used in cycling to induce Zintl phase formation was Gen2 + 10% FEC + Mg(TFSI)$_2$. Samples were prepared according to a sample and electrolyte preparation protocol developed by Jack Vaughey, Baris Key, and Binghong Han at ANL. The original Si electrode material was composed of 80% Paraclete Si nanoparticles, 10% conductive carbon, and 10% binder. The full cycle was carried out in a half cell against Li/Li+ between 0.01 and 1.5 V at a rate of C/20, with a voltage hold at 0.01 V during the lithiation process.
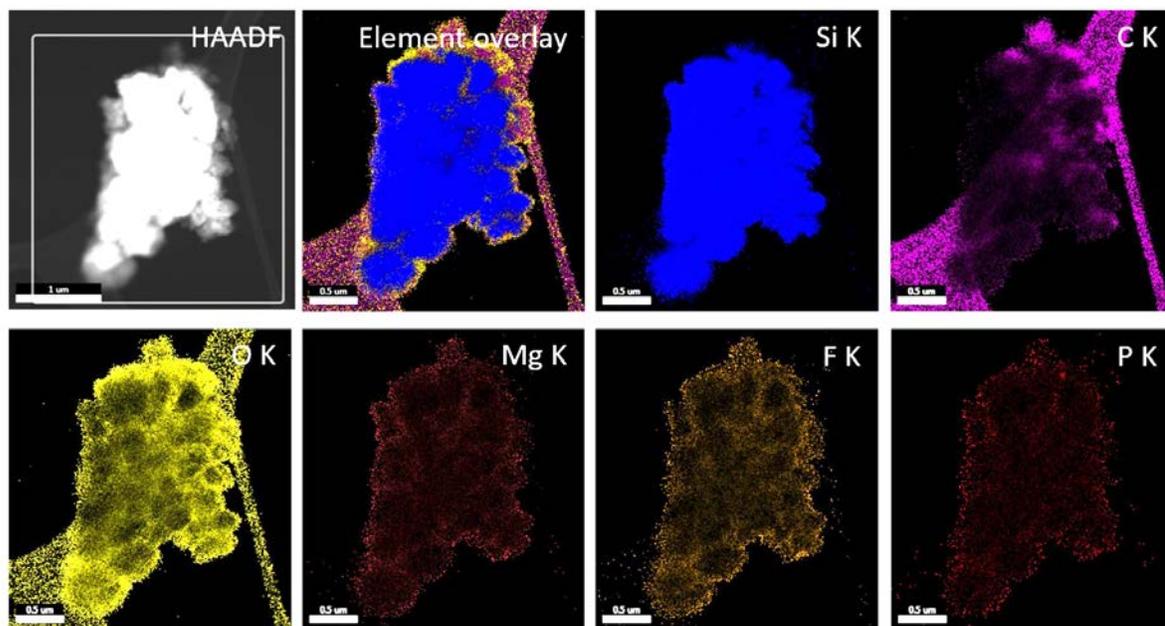
Figure 3. STEM of Zintl phase materials formed on Si composite electrode. Elemental maps obtained via energy-dispersive X-ray spectroscopy (EDS) include Si K, C K, O K, Mg K, F K, and P K.

6

STEM results depicted a composite electrode structure after Zintl phase formation. Si remains the primary element distributed throughout the electrode particles, but a shell appears representative of the surface composition, including high relative composition of O, Mg, F, and P.

AFM measurement of these materials showed a rough morphology incompatible with measurement of electronic properties via scanning spreading resistance microscopy (SSRM). Future scanning probe microscopy (SPM) experiments on Zintl-phase materials formed on a flat Si anode may be capable of determining the depth and electronic conductance of Zintl phase formation.

Conclusions

Characterization of late-stage SEI was carried out with AFM and SSRM. After 700 cycles, SEI thickness increased modestly from 50 cycles whereas roughness increased significantly.

Zintl phase materials were characterized via STEM and AFM. STEM showed an O-, Mg-, F-, and P-rich shell formed at the outside interface of the Si electrode particles.

Computational Determination of the Silicon/Electrolyte Interface

Kristin Persson (University of California Berkeley)

Background

Previously, the SEISta consortium identified the native SiO_2 as playing a major role in the surface behavior and passivation of the silicon anode. Experiments have shown a non-passivating behavior and corrosion current at high voltages, well above the predicted lithiation of SiO_2 and Si. Building on previous work by Aykol et al. [1], who studied competition between amorphous Al_2O_3 and crystalline α-Al_2O_3 and γ-Al_2O_3, we study the stability of the amorphous SiO_2 native oxide layer and elucidate the impact of the confining effects of a film, versus the bulk, on the lithiation behavior of the native oxide.

Based on our previous simulation work on the influence of FEC on the solvation structure of EC electrolyte, we continue our work to include EMC, as used in the Gen2 electrolyte, to study how linear carbonate additions affect the properties of the electrolyte. Here, we compare the difference in solvation structures between the EC electrolyte and the Gen2 electrolyte. Furthermore, the solvation structures will serve as an input for the future study of the SEI formation reactions with Gen2 electrolyte.

Results

To study the thermodynamics of nanometer-thick SiO_2 films, we used VASP calculations with ~10 Å of added vacuum. Using this approach, we are able to systematically generate slabs of Si and SiO_2, create interfaces, and calculate density function theory (DFT) energies of each slab termination/junction. First, before generating interfaces, we examine the slabs of Si and SiO_2. From the Materials Project, we find the majority surface facet of Si to be (111). This facet has two possible terminations: 1) one high-density surface leaving one dangling bond per surface Si and 2) one low-density termination with three missing bonds per Si. As expected, we find the higher Si density plane to exhibit the lowest energy. Likewise, with SiO_2, we find two inequivalent surface terminations: 1) one symmetric O-terminated slab and 2) one asymmetric O- and Si-terminated slab. Upon relaxing the atomic positions, we observe large geometric changes of the surface Si and O, ultimately indicating that SiO_2 prefers oxygen terminations, as shown in Fig. 1a. Interestingly, this changes when H is added to the surface near surface atoms with unsaturated bonds. The surface geometry is largely intact, and the asymmetric slab becomes the more stable, as depicted in Fig. 1b.
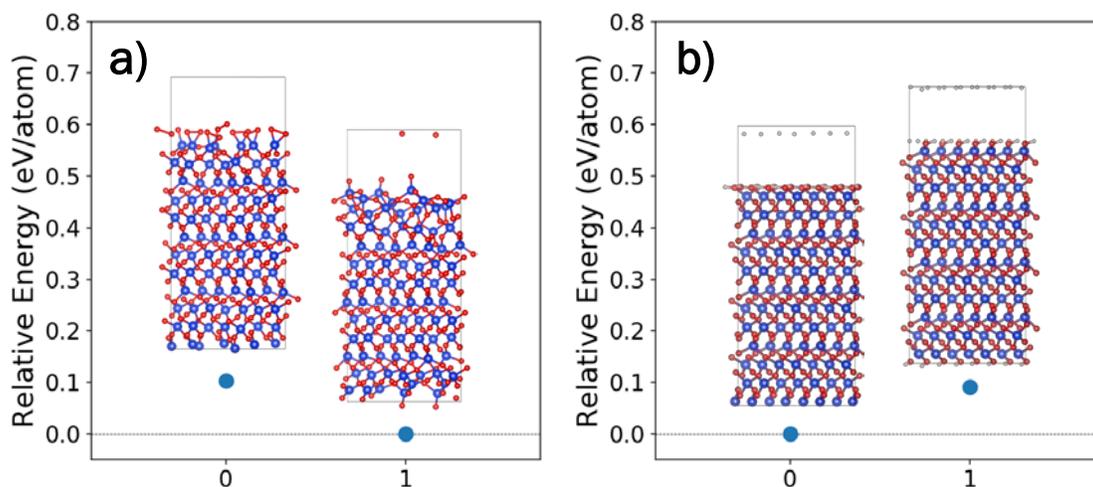
Figure 1. Relative energy of two terminations of stoichiometric SiO_2 a) with and b) without hydrogen surface terminations.

From the unit cells and slabs, epitaxial matches can be identified as described by Zur et al. [3]. Using the algorithm proposed by Zur et al., we identify two low-strain epitaxial matches between SiO_2 and Si: 1) SiO_2 (001) and Si (111) and 2) SiO_2 (110) and Si(100). Generating the interface and varying the thickness of the SiO_2 layer, we find that SiO_2 (001) and Si (111) form the lowest-energy interface, as shown in Fig. 2.
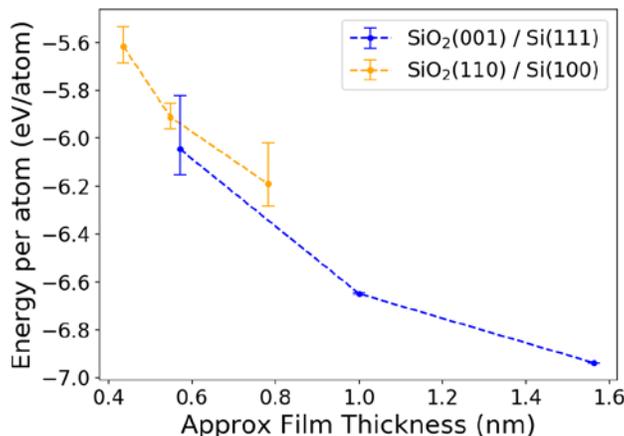
Figure 2. Energy per atom of two relaxed crystalline interfaces between 1) SiO_2 (001) and Si (111), and 2) SiO_2 (110) and Si (100) as a function of SiO_2 film thickness.

Expanding upon our previous work on amorphous SiO_2 and Si anodes, we also generate amorphous SiO_2 films and amorphous SiO_2/Si interfaces with varying SiO_2 film thicknesses and compare the energies with the crystalline films. Similar to the results found by Aykol et al. [1], we find an amorphous film to be preferred for thin films, with a crystalline film preferred when > 0.3 nm.
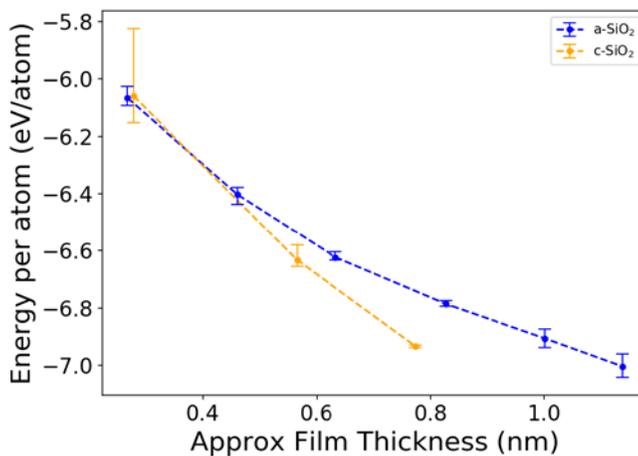
Figure 3. Energy per atom of interfaces between 1) amorphous SiO_2 and 2) crystalline SiO_2 (001) with Si (111).

The solvation structures of EC and Gen2 electrolyte are compared by conducting molecular dynamics simulations for EC (1.2 M $LiPF_6$ in EC) and Gen2 (1.2 M Li in EC:EMC (v/v 3:7)) electrolytes. Figure 4 shows the three representative solvation structures for Gen2 electrolyte, which are solvation-separated ion pairs (SSIP), contact ion pairs (CIP), and aggregate (AGG). For all three structure categories, EC and EMC both participate in forming the first solvation shell. Meanwhile, both EC and EMC coordinate with Li^+ ions via the carbonyl oxygen but not the alkoxy oxygen.

9

Solvent separated ion pairs (SSIP)   Contact ion pairs (CIP)   Aggregates (AGG)
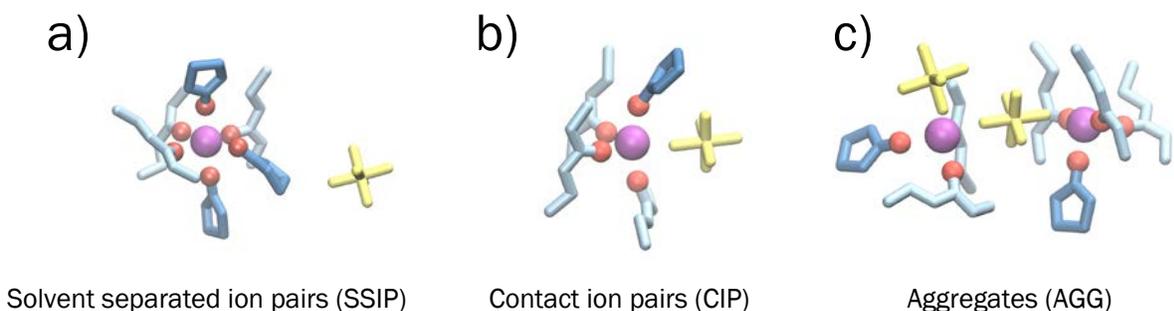
Figure 4. Three representative solvation structures in Gen2 electrolyte. a) Solvation-separated ion pairs (SSIP), b) contact ion pairs (CIP), and c) aggregate (AGG). The light blue, dark blue, and light yellow line representations denote the EMC, EC, and PF_6^- clusters, respectively. The purple- and red-ball representations denote Li ions and coordinating carbonyl O atoms, respectively.

These three solvation structures also appear in the EC electrolyte, but the proportion of each category changes between EC and Gen2 electrolyte, as analyzed by the molecular dynamic statistics. For the EC electrolyte, 86.95% of the Li ions form SSIP, whereas in Gen2 electrolyte, SSIPs only make up 36.81% of the total Li+ ions. CIP and AGG constitutes 31.79% and 31.4% in Gen2 electrolyte—meaning that in the Gen2 electrolyte, the Li^+ cations and PF_6^- anions are more associated, whereas CIP and AGG represent 11.03% and 2.02% in pure EC. The higher SSIP population in the EC electrolyte indicates that the EC electrolyte has more ionic conduction carriers than the Gen2 electrolyte.
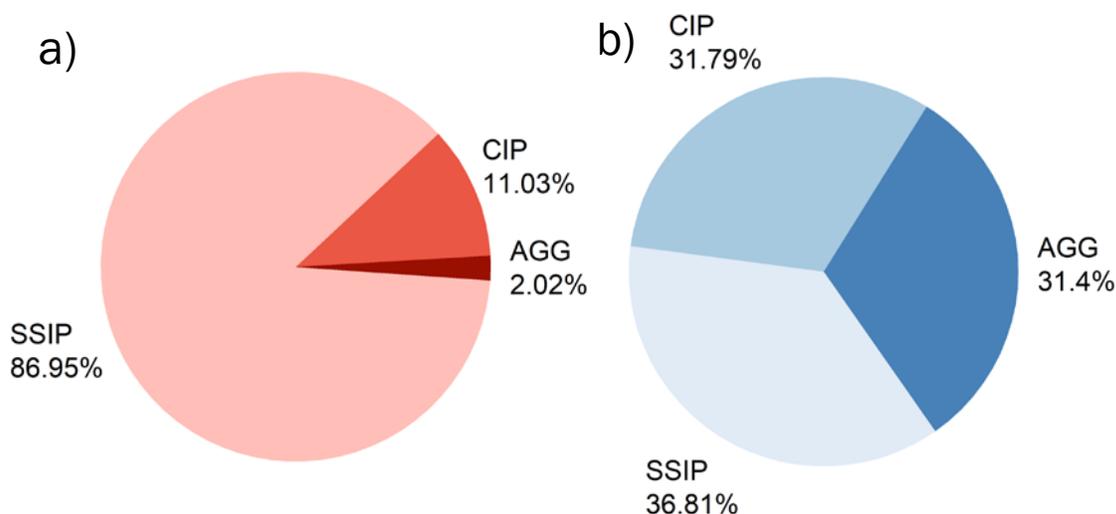
Figure 5. The proportions for SSIP, CIP, and AGG in the a) EC electrolyte and b) Gen2 electrolyte.

The averaged solvent coordination number for these three species are also statistically analyzed. For both the EC and Gen2 electrolyte, the total solvent coordination number decreases as one PF_6^- coordinating with Li to form CIP and more PF_6^- coordinating with Li to form AGG. Interestingly, in the Gen2 electrolyte, only the coordination number for EC decreases whereas that for EMC is preserved between species, indicating that the EC molecules are substituted by PF_6^-. This may be attributed to the bulky shape of EMC, which results in

larger Lennard-Jones forces that confine or stabilize the coordinating structure and renders EMC-Li+ a stiffer configuration. More detailed study of this phenomenon will be conducted in the future.
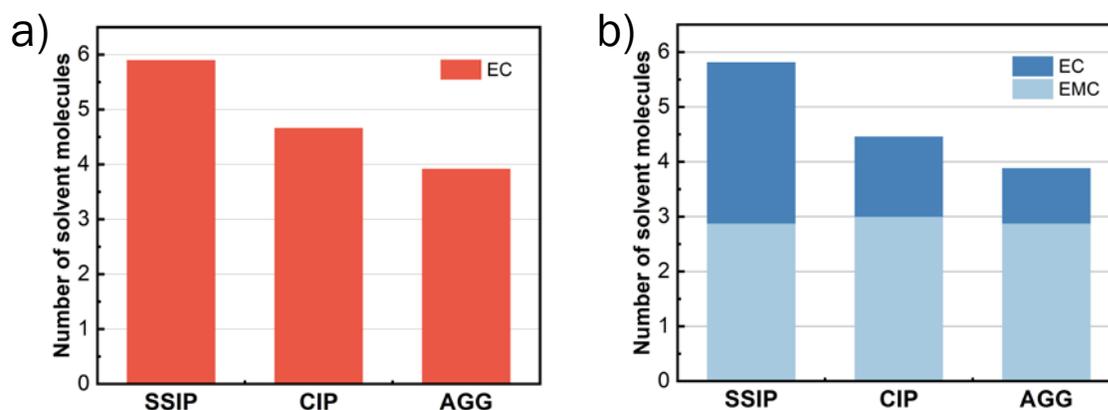
Figure 6. The coordination number of solvent molecules for SSIP, CIP, and AGG species in a) EC electrolyte and b) Gen2 electrolyte.

Conclusions

Our studies show that an amorphous oxide layer is preferred over a crystalline oxide in early stages of film growth. However, after ~0.3 nm, the crystalline film is thermodynamically favored. The fact that amorphous oxide films are observed in nm-thick SiO_2 suggest that the crystallization of the early-stage oxide is kinetically hindered and the growth conditions favor the amorphous configuration.

The Gen2 electrolyte favors much higher CIP ratio (>30%) and AGG ratio (>30%), whereas the EC electrolyte exhibits nearly 90% SSIP and 10% CIP. Hence, the EC electrolyte presents more ionic conduction carriers as compared to the Gen2 electrolyte. The EC molecule is substituted by PF_6^- for both EC and Gen2 electrolyte when forming CIP and AGG.

References

1. Aykol, M. & Persson, K. A., Oxidation protection with amorphous surface oxides: Thermodynamic insights from ab initio simulations on aluminum. *ACS Appl. Mater. Interfaces* **10,** 3039–3045 (2018).
2. Tran, R. *et al.,* Surface energies of elemental crystals. *Sci. Data* **3,** 160080 (2016).
3. Zur, A. & McGill, T. C., Lattice match: An application to heteroepitaxy. *J. Appl. Phys.* **55,** 378–386 (1984).

Lithiation of Silicon Wafer Anodes with SiO_2 Coatings (NREL)

Manuel Schnabel (NREL) and Paul Stradins (NREL)

Background

In this report, we describe results obtained on Si wafer anodes with 1.3–5.0-nm SiO_2 coatings, prepared by thermally growing SiO_2 of the desired thickness on Si in an N_2:O_2 ambient at 850°C. The anodes were characterized in half-cells using the O-ring cells presented earlier, which restrict the electrochemically active area to the oxidized front surface of the wafer and eliminate edge effects. This time, we try to answer the question, "Is oxide beneficial for the lithiation?," focusing on microscopic insights.

Results

Previously, we reported the effect of 1.4–5.2-nm thermal SiO_2 coatings on the lithiation of Si wafers. Galvanostatic cycling was performed at 20 μAcm^{-2} in Gen2 electrolyte against Li metal counter and reference electrodes with no lower voltage cut-off. From the electrochemical data, a stark difference was observed between samples with less than 3.0-nm SiO_2 and more than 3.0-nm SiO_2. Namely, for samples with less than 3.0-nm SiO_2, their cycling curves typically overlap already after the 2nd cycle, and their Coulombic efficiencies overlap at over 99%. Photographs of cycled samples indicated uniform lithiation.

Here, we studied the changes in Si, Li, O, and F bonding by X-ray photoelectron spectroscopy (XPS) for thin (up to 2.6 nm) oxide overlayers, and morphology of two-dimensional (2D) chemical composition changes in Si samples with thick (~ 5-nm) SiO_2 using time-of-flight secondary-ion mass spectrometry (TOF-SIMS) mapping. The XPS results for the two thin SiO_2 layers are compared in Fig. 1.
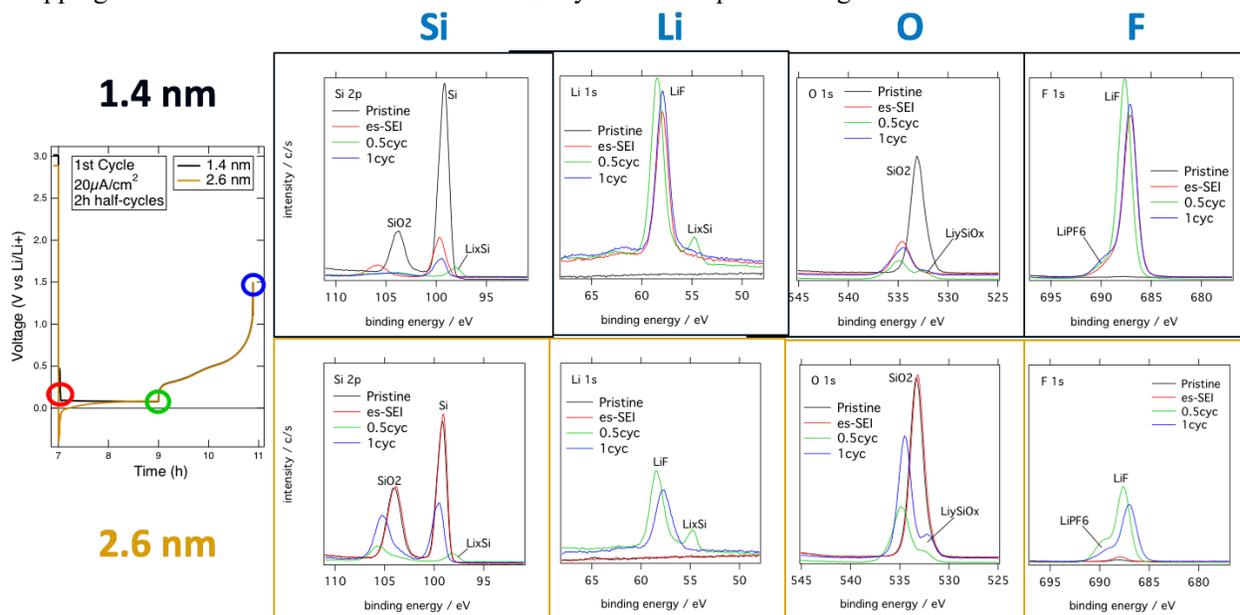
Figure 1. Changes in Si, Li, O, and F bonding studied by XPS. Colors of the XPS curves correspond to the lithiation-delithiation stages in the voltage-time plot on the left (two half-cycles, 2 h each).

From Fig. 1, we conclude that 1) 2.6-nm SiO_2 blocks pre-lithiation SEI because the SiO_2 remains visible after 1 full cycle; 2) silicon wafer lithiates reversibly ($LiSi_x$ peak appears and disappears), whereas the conversion of silicon oxide to a lithium silicate $SiO_2 \rightarrow Li_xSiO_y$ is not reversible.

In contrast, samples with >3.0-nm SiO_2 overlayer initially only lithiated at negative voltages vs Li and exhibited low Coulombic efficiencies, and photographs of cycled samples show only localized lithiation or Li plating. However, by the 9th cycle, their Coulombic efficiency increased and cycled at positive VLi, although at a higher residual resistance. This highly localized character of lithiation suggested a pinhole-type mechanism. It is not yet clear if the pinholes initially exist in the thick SiO_2, or if they appear as the result of nonuniform reaction of Li with the SiO_2. In addition, it appeared from the optical photographs that each localized lithiated spot (with pronounced change in the relief) also had a pronounced contrast change in its vicinity—extending farther away from the relief and suggesting possible lateral Li penetration below the thick SiO_2. To test this hypothesis, we performed TOF-SIMS 2D compositional mapping around the lithiated spots. The results are shown in Fig. 2 and clearly show that Li has spread massively over a much larger sample area than indicated by the optical contrast. From these 2D maps alone, it is not possible to attribute Li spreading to within the wafer (underneath the SiO_2) or first lithiating the SiO_2 overlayer. However, 2D depth-profile maps (not shown) indicate that Li had first entered the Si wafer through the pinholes and had then spread underneath the thick SiO_2.

These results were reported at the ECS 2019 meeting in May by Manuel Schnabel.
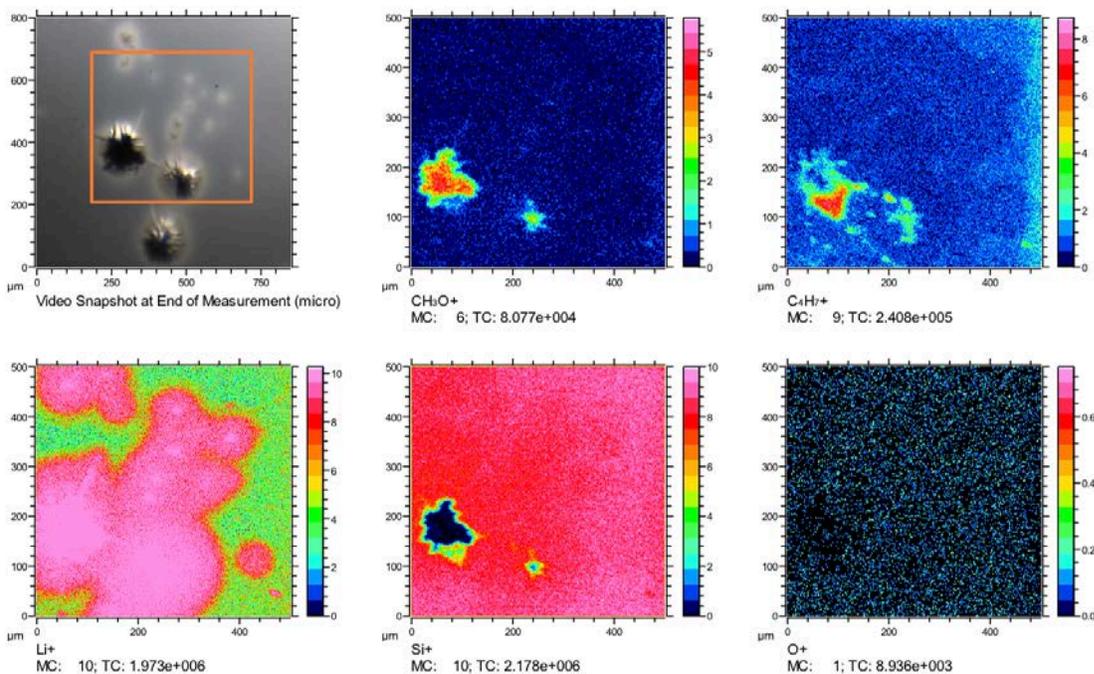
Figure 2. Two-dimensional TOF-SIMS map of Li, Si, O, and carbon-containing sputtering fragments, along with the optical micrograph. The mapping area was 500x500 microns and is shown in the micrograph by the orange contour.

Conclusions

- Transition between uniform and localized lithiation occurs at ~3.0-nm SiO_2 thickness.
- At oxide thickness <3.0 nm: uniform lithiation at 20 $\mu A/cm^2$ or at 0.01 V_{Li}.
- At thickness >3.0 nm: localized lithiation, <0 V_{Li} at 20 $\mu A/cm^2$, exponentially rising current at 0.01 V_{Li}.
- Localized lithiation proceeds through SiO_2 pinholes, local decrease in SiO_2, Li spreading beneath SiO_2.

Part 2. SEI Stability

Chemical and Electrochemical Reactivity of Plasma-Synthesized Silicon Nanoparticles

Mike Carroll, Greg Pach, Fernando Urias-Cordero, Ryan Pekarek, Bertrand Tremolet de Villers, Nathan Neale (NREL)

Background

One of NREL's tasks explores plasma-synthesized silicon nanoparticles (Si NPs) as model systems for Li_xSi anodes. Such plasma-prepared Si NPs are valuable because they feature hydrogen-passivated surfaces and a high surface area resulting from their <10-nm diameter that makes them well suited for chemical reactivity studies using Fourier transform infrared (FTIR) spectroscopy and quantitative off-gassing analysis. These reactivity studies are relevant for understanding 1) early-stage SEI layer growth as well as 2) individual SEI component chemical stability. In FY19, we continued our prior years' efforts to 1) develop an *operando* attenuated total reflection (ATR)-FTIR capability for studying early-stage SEI grown and dissolution; 2) increase the size and scale of our Si NP plasma production process; and 3) started a new effort to incorporate plasma-grown Si NPs into batteries.

In Q3 FY19, we finally achieved our long-sought goal of implementing the *operando* ATR-FTIR tool for experiments on early-stage SEI growth (development of this capability was completed in Q2 FY19). We continued to prepare many batches of plasma-synthesized Si NPs over a range of moderately small (5–25 nm) diameters to support internal battery electrode fabrication as well as collaboration with ANL. Finally, we have collected half-cell battery data for air-free electrodes prepared with small-diameter, plasma-grown Si NPs that definitely show that SiO_2 does not contribute to appreciable capacity in Si NP-based anodes.

Results

Operando ATR-FTIR Spectroscopy. In Q3 FY19, we have implemented our *operando* ATR-FTIR spectro-electrochemical instrument in experiments probing early-stage SEI growth. Figure 1 (left) displays representative data of cycling data from 1.5 to 0.01 V, demonstrating the high-quality electrochemical response provided by our critical Q2 FY19 breakthrough—the surface p+-doped Si wafer. These data also demonstrate that substantial current is passed prior to the crystalline Si lithiation potential (~115 mV) indicative of SEI growth.
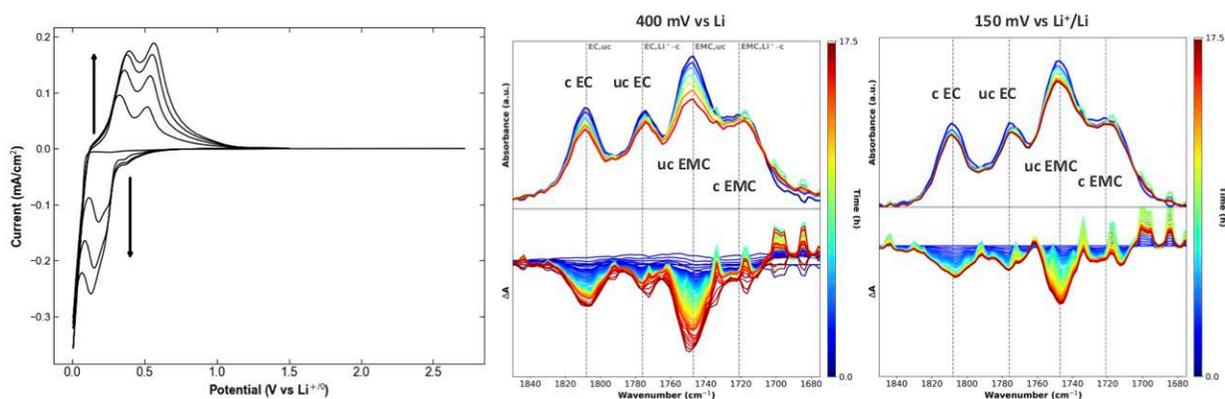
Figure 1. Left: Cyclic voltammagrams for heavily surface p+-doped Si wafers (bulk resistivity 5–10 $\Omega\cdot$cm) in the ATR-FTIR spectro-electrochemical cell. These surface-doped wafers feature a ~100-nm-deep surface p+ layer (doping density 10^{19}–10^{20} cm^{-3}) resulting in a highly conductive working electrode (<1 m$\Omega\cdot$cm). ATR-FTIR spectra and difference spectra of the

carbonyl region under potentiostatic holds at 400 mV (Middle) and 150 mV (Right) over 17.5 h, showing preferential loss of uncoordinated "uc" EMC.

Our initial experiments have directly targeted the SEISta FY19 Milestones by conducting potentiostatic holds at a range of potentials (OCV, 1.0 V, 0.7 V, 0.4 V, 0.15 V, 0.1 V vs. Li$^{+/0}$) on native SiO$_x$-terminated p$^+$-Si wafers. We find that at 0.1 V vs Li$^+$/Li, lithiation of the Si wafer anode quickly eliminates its reflective nature and the ATR-FTIR signal is lost. Given the cyclic voltammagrams from Fig. 1 (left) showing that minimal current is passed at potentials higher than 0.5 V vs. Li$^{+/0}$, we focused on the low-potential regions of 0.4 and 0.15 V vs. Li$^{+/0}$. First, the spectra collected during these potentiostatic holds (Fig. 1, middle and right) show dynamic behavior throughout the course of the experiment, suggesting that the SEI continues to grow at these potentials over the 17.5 h experiment. Second, over the entire full spectral range (500–4000 cm^{-1}), no new peaks are observed. Third, the intensity of the raw vibrational absorptions changes only slightly, with difference spectra required to observe the modulation of individual peaks. These latter two results show that the evanescent wave penetrates significantly into the electrolyte (concurring with the works of Komvopoulos and coworkers[1] showing the penetration depth of 50–500 nm, depending on the functional group and angle of the incident FTIR beam). Thus, in the present configuration of a combined substrate and working electrode wafer Si, this *operando* ATR-FTIR experiment is probing near-surface changes to the electrolyte, *not* the SEI itself.

Still, these data clearly show that uncoordinated EMC is preferentially lost in the near-surface electrolyte region. Whether this is due to direct decomposition or by decomposition of Li$^+$-coordinated EMC (where uncoordinated EMC replaces lost Li$^+$-coordinated EMC due to Le Chatelier's principle) is unclear, and further experiments will be required to evaluate the mechanistic details. Regardless of mechanism, this is an exciting result because it points to the organic constituents in the Gen2 electrolyte that result in early-stage SEI growth. Future work will 1) detail cycling behavior from 0.15 and 0.40 V to 1.5 V, which is expected to reveal the electrolyte response to dissolution and growth; 2) conduct a series of corollary potentiostatic hold and cycling experiments on H-terminated as well as molecularly functionalized p$^+$-Si wafers; and 3) probe complete Si NP-based electrodes on the p$^+$-Si wafer substrate. This third set of experiments in particular will allow us to probe the actual SEI, not just the electrolyte, as well as the SEI that is formed upon lithiation. These experiments will be enabled by our work on using plasma-synthesized Si NPs under air-free conditions in battery electrodes as well as our ability to control the crystallinity of the Si NPs via the plasma growth process. Amorphous Si can be lithiated at more positive potentials (~0.4 V vs. Li$^{+/0}$) than crystalline Si (~0.115 V vs. Li$^{+/0}$), so we can perform the same potentiostatic and cycling experiments and lithiate amorphous Si NP-based electrodes without lithiating the underlying p$^+$-Si wafer substrate.

Silicon Nanoparticle Production via Nonthermal Plasma Synthesis. In Q3 FY19, we focused primarily on growth rate and now regularly grow gram-scale quantities of ~4- to ~25-nm-diameter Si NPs. One of these samples (7-nm diameter, 1 g) was shipped by John Zhang at ANL for our continued collaboration.[2] Other batches of Si NPs were stockpiled in preparation for numerous experiments on battery electrodes conducted by NREL employee postdoctoral researchers as well as two summer undergraduate interns.

Generating this stockpile was necessary because we have spent a large fraction of Q3 FY19 working on maintenance and upgrades to our RF-enhanced nonthermal plasma reactor. Our original 10% silane in helium (SiH$_4$/He) gas cylinder reached its 7-year anniversary in May. NREL rigorously follows the semiconductor gas industrial standard protocols that require cylinders to be replaced every 7 years. To improve our ability to grow Si NP size and scale, we decided to leverage our existing 100% SiH$_4$ line and splice it to supply two different mass flow controllers and a separate 100% He source. In this way, we can make custom blends of the gas during our growth runs, which should allow us access to greater sizes and greater scales than with our previous 10% pre-blended cylinder.

Shutting down our system for this hardware maintenance is no simple task, requiring 2–3 weeks of coordination, planning, and work with our environment, safety, health, and quality (ESH&Q) staff, among others. Thus, we also decided to upgrade our system by adding two additional organometallic bubbler sources.

One source is tetramethyltin (TMT), which will allow us to grow SiSn alloys—allowing our plasma system to complement Robert Kostecki's SPLAT SiSn alloy fabrication at LBNL in FY20. The second source currently is planned for dimethylzinc (DMZ), which will support work on another project. However, another possibility would be to switch out the DMZ precursor with a volatile magnesium (Mg) precursor, such as bis(cyclopentadienyl)magnesium (Cp$_2$Mg), and perform a surface-doping study akin to Jack Vaughey and Baris Key's experiments at ANL that appear to stabilize Si NP-based anodes under cycling conditions.

Understanding the Role of Silicon Dioxide and Other Si NP Surface Chemistries in Silicon NP Batteries. In an expansion of this portion of the SEISta project, a major effort in FY19 has been undertaken to correlate SEI early-stage growth and dissolution with performance of Si NPs in batteries. Our goal is to study surface-functionalized Si NPs fabricated into batteries *air-free*, and in doing so, to understand how the Si NP surface bonding structure impacts the evolution of the SEI and stability of the electrodes as well as deconvoluting the impacts of oxide vs surface chemistry.

At our quarterly meeting on July 8, 2019, we will give a full update on the extensive progress we have made in this area. *The executive summary is that our Q3 FY19 experiments unequivocally prove the hypothesis that silicon dioxide (SiO$_2$) is highly detrimental to the capacity and cycling stability of Si NP-based anodes.* Notably, this hypothesis did not arise in a vacuum, and it has been enabled by the entire SEISta team working on model systems over the past nearly 3 years (see AMR presentation).

Slurries were prepared using in-house purified polyacrylic acid (PAA) binder and dried Timcal C65 conductive carbon in purified N-methyl-2-pyrrolidone (NMP) solvent. Slurries of plasma-grown 4–7-nm Si NPs were contained a very low amount of Si NPs relative to C65 conductive carbon based on the percolation theory framework that sets a lower limit on the ratio of conductive carbon/Si NPs. With the small 4–7-nm-diameter Si NPs in this investigation, it is important to emphasize that electrodes comprise 75%–80% C65, and thus, these are not commercially viable electrodes because their overall capacity by total mass is quite low. We have embarked upon a series of experiments that explore this electrical percolation limit to provide the framework for an optimized electrode formulation based on the conductive carbon/Si NP ratio.

We first probed our pre-treatment of the Si NPs in NMP solvent developed in Q2 FY19. As shown in Fig. 2 (left), the FTIR spectra following exposure to NMP results in a substantial change to the spectrum, including a large peak in the Si–O stretching region. Based on our prior published work on the reactivity of Si NPs,[3,4] we would expect that a surface radical reaction will occur with oxygen donors results in a surface *Si–O bond (in this case, the carbonyl group of NMP such that the surface functionality is likely *Si–O–C). Thus, it is impossible to deconvolute any trace oxidation that would occur during this chemical exposure from the Si–O stretch that is generated by reaction with NMP. We then turned to X-ray photoelectron spectroscopy (XPS) to quantify the degree of oxidation that occurs following this pre-treatment. Figure 2 (right) displays XPS data collected at NREL showing that only minor oxidation occurs in the NMP-processed sample based on the major Si^0 peak versus the minor Si^{4+} peak (blue spectrum). In contrast, the same Si NPs processed in water show complete oxidation in the same Si 2p XPS region (red spectrum)—that is, no Si remains and these small-diameter NPs are fully converted to SiO$_2$. Interesting, a sample of the 4KD batch of Paraclete (green spectrum) shows that a large proportion of the Si in these commercial Si NPs exists as SiO$_2$.
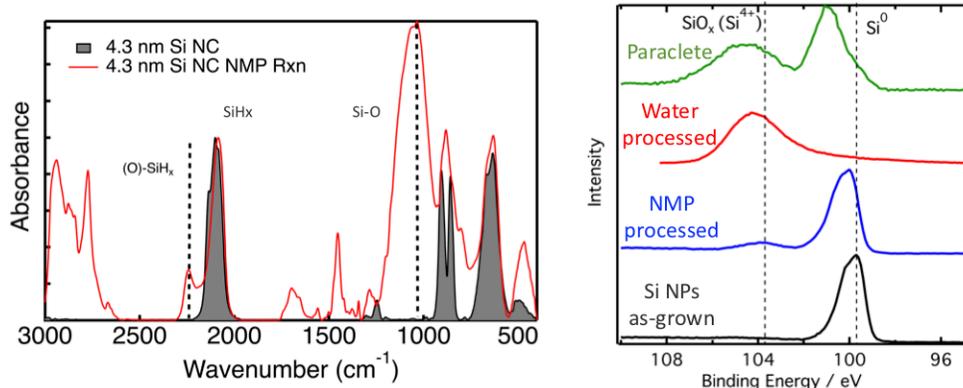
Figure 2. Left: FTIR data from plasma-synthesized Si NPs (gray-shaded spectrum) as-prepared and (red) following pre-treatment in NMP solvent. Right: XPS data for Si 2p region for Si NPs (black) as-prepared, (blue) following pre-processing in NMP solvent, (red) following pre-processing in water, and (green) Paraclete as comparison.

Si NPs pre-treated with NMP and H_2O (the latter termed SiO_2 based on the XPS data) were fabricated into half-cell batteries as described in our Q2 FY19 report. Three forming cycles were conducted at C/20 between 1.5 and 0.1 V, and the measurement cycling protocol was 1 C between 1.5 V and 0.1 V. We additionally conducted the identical experiments on Timcal C65 alone to quantify the capacity of the conductive carbon. We can thus subtract the capacity of the C65 (which again represents the bulk of the electrode active material) and obtain the capacity of the Si (or SiO_2) alone and plot that in Fig. 3 (left). These data show that the C65 and SiO_2 each contribute small capacities over 50 cycles (black and red data). In contrast, NMP-processed Si NPs fabricated into electrodes under air-free conditions exhibit substantial and stable capacity approaching 3000 mAh/g_{Si+C65} (blue data). Corroborating this capacitance and Coulombic efficiency data are the dQdV plot of the 1st cycle for all three samples, which demonstrates that the air-free processed Si is the only sample to undergo reversible lithiation and delithiation. *This result provides clear evidence that any Si that is oxidized to SiO_2 is ineffective in contributing substantially to the capacity of a Si-based anode. Further, any commercial effort using Si NP-based anodes should focus on oxide-free material*, which is far from the industrial or research standard. Our future work will focus on extending these studies to a larger range of Si NP sizes as well as exploring various surface chemistries that can enhance the Coulombic efficiency of these minimally oxidized Si NPs.
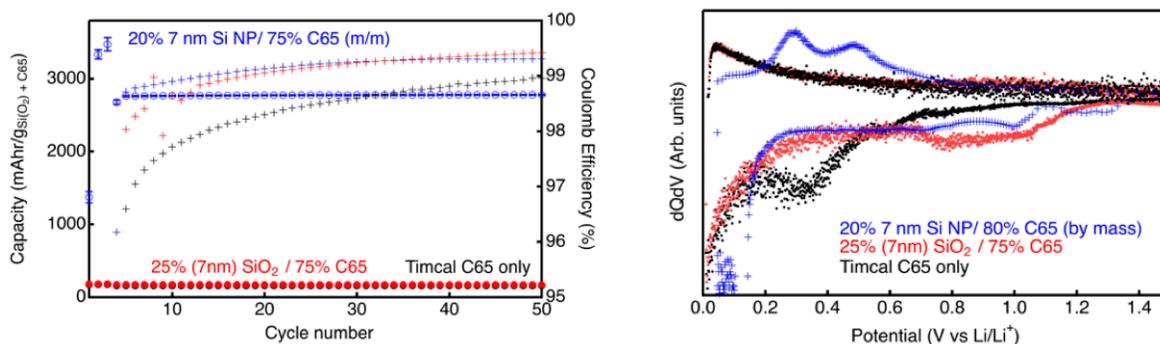
Figure 3. Left: Capacity and Coulombic efficiency of half-cell anodes made from plasma-grown Si NPs (blue) fabricated (blue) air-free using NMP solvent or (red) in air using H_2O solvent with C65, or (black) with C65 alone (i.e., no Si). Right: Normalized dQdV versus potential plot of the 1st cycle of the same samples showing that only the air-free-processed Si NP electrode undergoes reversible lithiation and delithiation.

Conclusions

Summary of Q3FY19 is:

- ATR-FTIR spectro-electrochemical experiments show that uncoordinated EMC is preferentially lost in the near-surface electrolyte region, which points to the organic constituents in the Gen2 electrolyte that result in early-stage SEI growth.
- Many grams of capacitively coupled Si NPs ranging in size from ~4- to ~25-nm diameter were prepared to support the Si Anode Consortium. Major upgrades to the system are underway.
- Half-cell battery data for air-free processed electrodes definitely show that SiO_2 does not contribute to capacity of Si NP-based electrodes. Future work should focus on samples without appreciable oxidation.

References

1. "The Chemistry of Electrolyte Reduction on Silicon Electrodes Revealed by in Situ ATR-FTIR Spectroscopy," Shi, F.; Ross, P. N.; Somorjai, G. A.; Komvopoulos, K. *J. Phys. Chem. C* **2017**, *121*, 14476.
2. "Tailoring the Surface of Nano Silicon Particles for Enhanced Chemical and Electrochemical Stabilities in Li-ion Batteries," S. Jiang, B. Hu, R. Sahore, H. Liu, G. M. Carroll, G. F. Pach, L. Zhang, B. Zhao, N. R. Neale, Z. Zhang, *Submitted* (2019).
3. "Tuning Quantum Confinement in Colloidal Silicon Nanocrystals with Saturated Surface Ligands," G. M. Carroll, R. Limpens, N. R. Neale, *Nano Lett.*, **2018**, *18*, 3118–3124.
4. "Intrinsic Reactivity of Solid-Electrolyte Interphase Components in Silicon-Lithium Alloy Anode Batteries," R. T. Pekarek, A. Affolter, L. L. Baranowski, J. Coyle, T. Hou, K. A. Persson, B. Key, C. Apblett, G. M. Veith, N. R. Neale, *In preparation* (2019).

The *In-Situ* Study of the Solid-Electrolyte Interphase Formation as a Function of the Binder Polyacrylic Acid

Katie L. Browning (ORNL, UTK) and Gabriel M. Veith (ORNL)

Background

We used neutron reflectometry (NR) to study how the polymeric binder, polyacrylic acid (PAA), mediates the formation and chemical composition of the solid-electrolyte interphase (SEI) formation at various states of charge. The thin-film architecture allowed for a controlled interface between the amorphous Si (a-Si) electrode and the PAA film on the anode surface. Neutron techniques are more deeply penetrating than X-rays, in addition to being sensitive to lighter elements such as Li and H. From the fits to the reflectivity data, the thickness, roughness, and/or diffuseness of the layers of the system can be determined, giving a better understanding of buried interfaces as a result of *in-situ* measurements. The most important parameter obtained is the scattering length density (SLD), which gives information on the composition of the layer. Refinements to the data resulted in a SLD plot—a one-dimensional representation of the heterostructures of the films as a function of SLD—separated by interfacial roughness.

Results

The PAA layer was spin coated to an average thickness of 28 nm on the surface of the vapor-deposited a-Si thin film. The cell was driven to potentials associated with SEI formation and lithiation of the a-Si thin-film electrode. Interestingly, when in contact with the electrolyte (1.2 M $LiPF_6$ in deuterated EC/DMC), the PAA swelled to a thickness of 36 nm. This is evidenced by both an increase in the PAA layer thickness and an increase in the SLD of the PAA from 1.8×10^{-6} $Å^{-2}$ in air to 4.3×10^{-6} $Å^{-2}$ in the deuterated electrolyte. In addition, a new layer is apparent on the surface of the anode—around 4 nm in thickness with a SLD of 1.53×10^{-6} $Å^{-2}$. The low SLD suggests a hydrogen-terminated oxide layer that has been previously observed on sputtered a-Si films.[1]
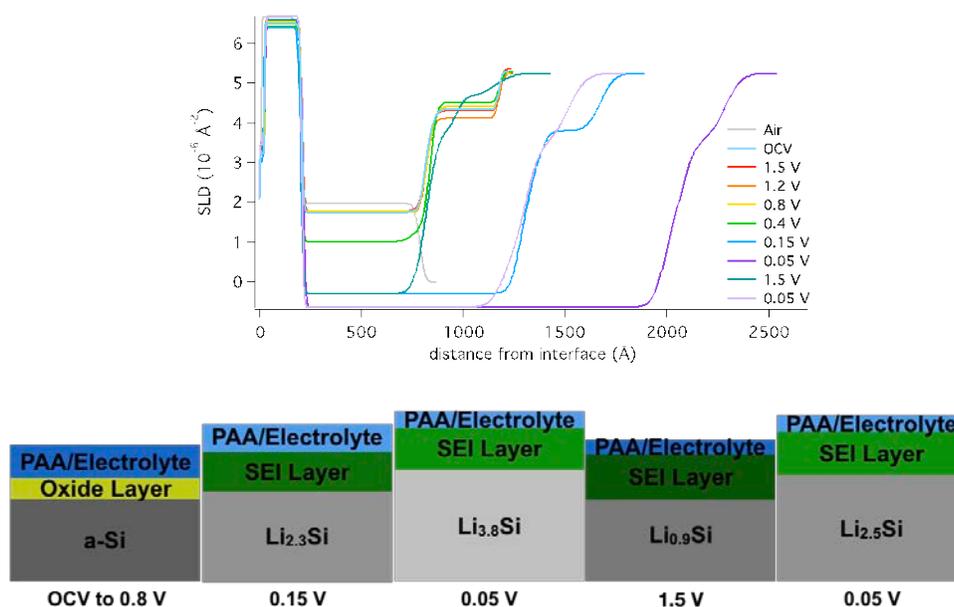
Figure 1. SLD plot of an a-Si thin-film electrode with spin-coated PAA binder (top) and a summary of the film heterostructures determined by NR refinements (bottom).

Interestingly, the oxide layer on the surface of the a-Si and the PAA layer at the electrolyte interface remain similar in chemical composition and thickness at OCV, 1.2, 0.8, and 0.4 V (Fig. 1 top: light blue, red, orange, and gold traces). The expected SEI formation at 0.8 V (vs. Li/Li$^+$) was not observed. Electrochemical quartz-crystal microbalance experiments confirm the NR refinements, indicating a stable viscoelastic response and minimal mass gain at the early potential holds. Lithiation of the a-Si begins at 0.4 V (vs. Li/Li$^+$) as evidenced by a decrease in the SLD of the a-Si layer as a result of Li incorporation into the film because Li is a negative scatterer (-1.90 fm). In relation to a previous NR experiment of a bare a-Si electrode in the same electrolyte system, a thick 25-nm organic SEI was observed as the solvent condenses on the surface of the electrode.[2] This was not observed with the PAA system, where the oxide layer remained at ~1.3×10^{-6} Å^{-2} and 5 nm in thickness. The PAA begins to thin, but similar in chemical composition from the OCV measurement. As the cell is further lithiated at 0.15 V (vs. Li/Li$^+$), the oxide on the surface of the a-Si increased in SLD from 1.52×10^{-6} Å^{-2} to 2.52×10^{-6} Å^{-2}, indicating the incorporation of heavier scatterers—most likely C, D, O, F, and P coming from the decomposition of the electrolyte resulting in formation of the SEI. The SEI is underneath the PAA layer on the surface of the lithiated Si and composed of inorganic species. Upon lithiation and delithiation, the SEI changes in chemical composition and thickness, resembling a "breathing" mechanism where SEI components are dissolved and reformed. The SEI thins during lithiation and thickens during delithiation. The increased SLD during delithiation indicates that the SEI becomes more organic. In the lithiated state, the SEI on the surface of the Si is ~10 nm thick and Li rich. The film heterostructures from the NR refinements are summarized in Fig. 1, bottom.

Conclusions

The effect of the binder, PAA, on the SEI formation and composition on the surface of an a-Si electrode was explored using *in-situ* neutron reflectometry. The full PAA coating of the a-Si resulted in little SEI formation up to 0.4 V (vs. Li/Li$^+$). The PAA forms an "artificial SEI" on the surface of the anode that mediates the chemical composition and thickness of the SEI layer until the start of lithiation (0.15 V). The SEI forms on the surface of the anode, underneath the PAA. The NR SLD plot indicates that the interface between the PAA and SEI is diffuse. In relation to processing conditions, a binder that fully coats the Si particle would form a different SEI than a patchy coating.

References

1. Veith, G. M. *et al.* Determination of the Solid Electrolyte Interphase Structure Grown on a Silicon Electrode Using a Fluoroethylene Carbonate Additive. *Sci. Rep.* **7**, 6326 (2017).
2. Veith, G. M. *et al.* Direct Determination of Solid-Electrolyte Interphase Thickness and Composition as a Function of State of Charge on a Silicon Anode. *J. Phys. Chem. C* **119**, 20339–20349 (2015).

Reactivity and Evolution of the Silicon-Electrolyte Interphase (SEI), Water Concentration Effect on SEI Thickness and Composition, and Nature of the Soluble SEI Components during Cycling (NREL)

Yeyoung Ha, Bertrand Tremolet de Villers, Caleb Stetson, Kae Fink, Chun-Sheng Jiang, Shriram Santhanagopalan, Mowafak Al-Jassim, and Sang-Don Han

Background

Due to complexity, high reactivity, and continuous evolution of the silicon-electrolyte interphase (SEI), the SiEI remains a poorly understood topic in advanced Li-ion battery research, and its detailed and real-time analysis is a great challenge. Vibrational spectroscopy is one of the most important avenues for understanding and quantifying the interfacial chemical and electrochemical reactions. In particular, Raman spectroscopy is attractive due to its versatility, and it is used extensively by the battery community in *ex-situ* form. Developing *in-situ* methods of this technique, however, will provide new insight and help to elucidate the mechanism of interfacial failure in battery systems. Another analytic technique to study degradation mechanisms in Li-ion batteries is gas chromatography-mass spectrometry (GC-MS). This has been used by others in the past to study electrolyte degradation and elucidate probable decomposition mechanisms.[1] Here, we attempt to use GC-MS to identify SEI components that dissolve in the electrolyte during cycling. In addition, water concentration in the electrolyte—one of the important factors to have an effect on SEI formation/evolution, and thus, electrochemical behavior of a cell—is controlled to determine how water concentration affects SEI thickness and composition. These studies can provide guidance to stabilize SEI by understanding the underlying chemistry and physics and providing a mechanical explanation of surface chemistry and various reactions/interactions within the SEI.

Results

I. Reactivity and Evolution of the Silicon-Electrolyte Interphase (SEI) – *in-situ* Raman Analysis

Reference Spectra and Peak Assignments. Figure 1 shows Raman spectra of neat solvent(s) and electrolytes: EMC (ethyl methyl carbonate, blue), 1.2 M LiPF$_6$ in EMC (orange), EC (ethylene carbonate)/EMC in 3:7 weight ratio (green), and 1.2 M LiPF$_6$ in EC (red). The spectra were collected with a 532-nm laser using the *in-situ* Raman cell only with electrolyte(s) or solvent(s). The observed peaks are assigned to vibrational modes of the uncoordinated and coordinated solvents (EC and EMC) and the salt (LiPF$_6$). We now have a complete set of electrolyte reference spectra and the updated peak assignment.

In-situ Raman Spectra during Electrochemical Cycling. For *in-situ* Raman measurements, a crystalline silicon wafer (c-Si, 525 μm, <0.005 Ω cm, p-type) strip and a lithium metal foil were used as the working and counter/reference electrodes, respectively. About 0.5 mL of standard Gen2 electrolyte (1.2 M LiPF$_6$ in EC/EMC (3:7, wt%)) were used to fill the cell. After two hours of rest at open-circuit voltage (OCV),
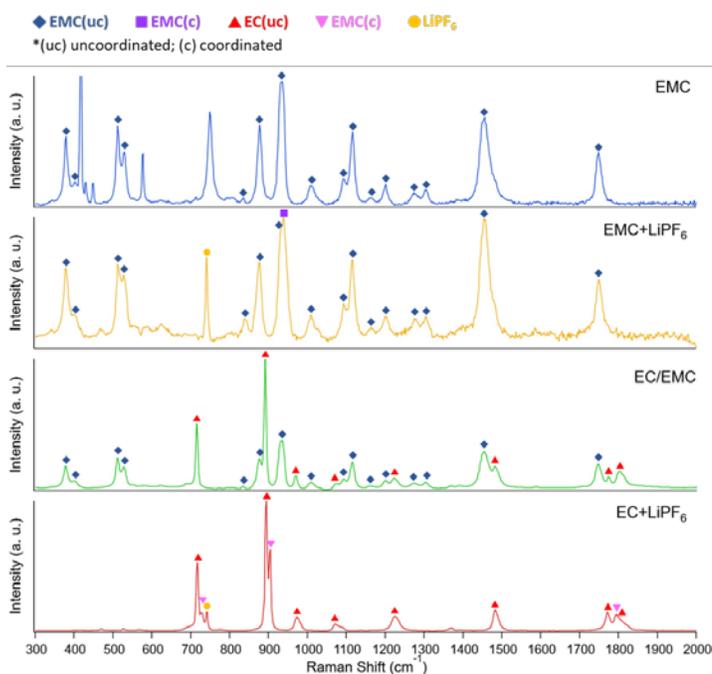
Figure 1. Reference spectra of EMC, 1.2 M LiPF$_6$ in EMC, EC:EMC (3:7, wt%), and 1.2 M LiPF$_6$ in EC collected with a 532 nm laser. Unassigned peaks are attributed to the sapphire window.

galvanostatic cycling was performed at 15 μA current with a voltage range of 0.01–1.50 V (*vs.* Li/Li$^+$, hereafter) for 5-hour half-cycle as shown in Fig. 2. Raman spectra were collected at different voltages for the 1st, 3rd, and 9th cycles.
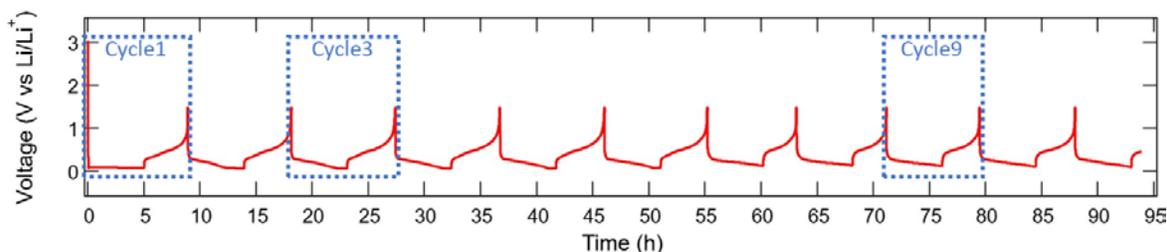
Figure 2. Electrochemical cycling performance of the *in-situ* Raman cell.

Previously, we observed the Si surface being damaged upon exposure to a laser beam. To alleviate beam damage, we defocused the laser beam by 30%, which disperses the laser beam to a larger area and reduces the intensity per unit area. In addition, we increased the slit width from 50 μm to 75 μm to compensate collection efficiency loss induced by defocusing the laser beam.

The voltage profile and optical images of a Si wafer at different stages during the 1st discharge/charge are shown in Fig. 3. During the 1st lithiation (discharge, 1–4), the voltage profile plateaus at around 100 mV, which is a typical behavior observed in previous cycling data with a crystalline Si. From the optical images, the Si wafer becomes darker as it is lithiated. During the 1st delithiation (charge, 5–10), two plateaus were observed in the voltage profile and the optical images show the Si wafer becoming brighter again. It is noted that we could not observe possible beam damages on the sample, so the laser defocusing method is effective to protect the sample and alleviate possible side reactions. The corresponding *in-situ* Raman spectra shows an interesting behavior, where the fluorescent background starts to decrease once the current is applied. The background continuously decreases during discharge, and it remains almost consistent during charge. Unfortunately, we could not observe any new peaks, induced from newly formed SEI components, in the spectra for the 1st cycle and even subsequent 3rd and 9th cycles (Fig. 4). However, the shape of the background (possibly caused by decomposed/reacted components) changed from the 3rd to the 9th cycle, indicating there are dynamic processes occurring.
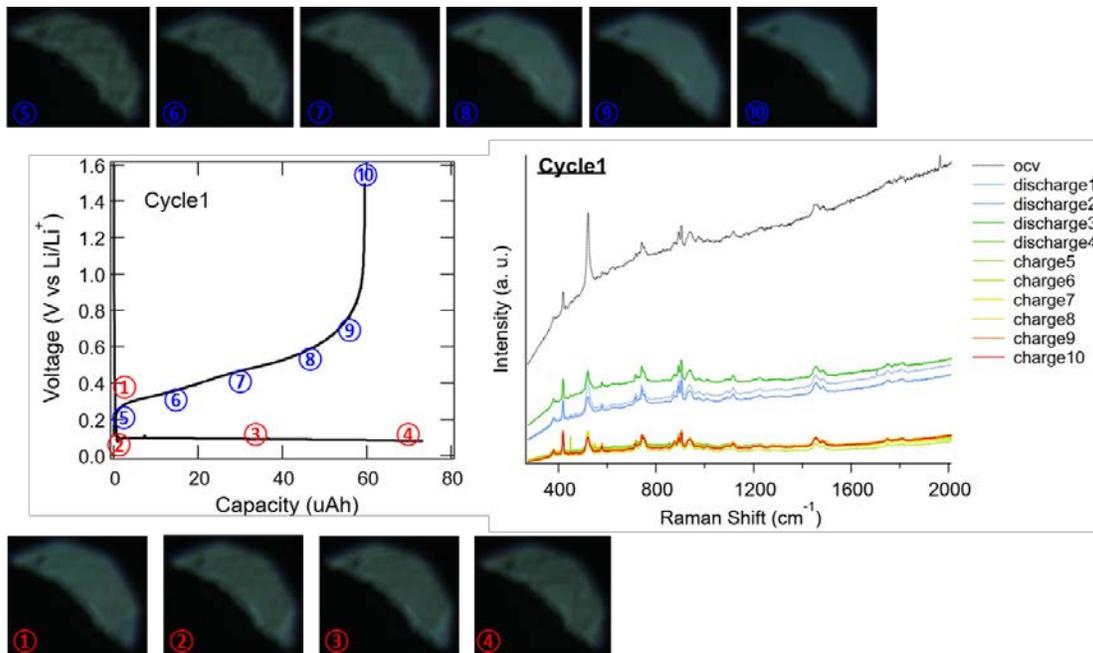
Figure 3. Voltage profile and corresponding in-situ Raman spectra and optical microscopy images for the 1st cycle.
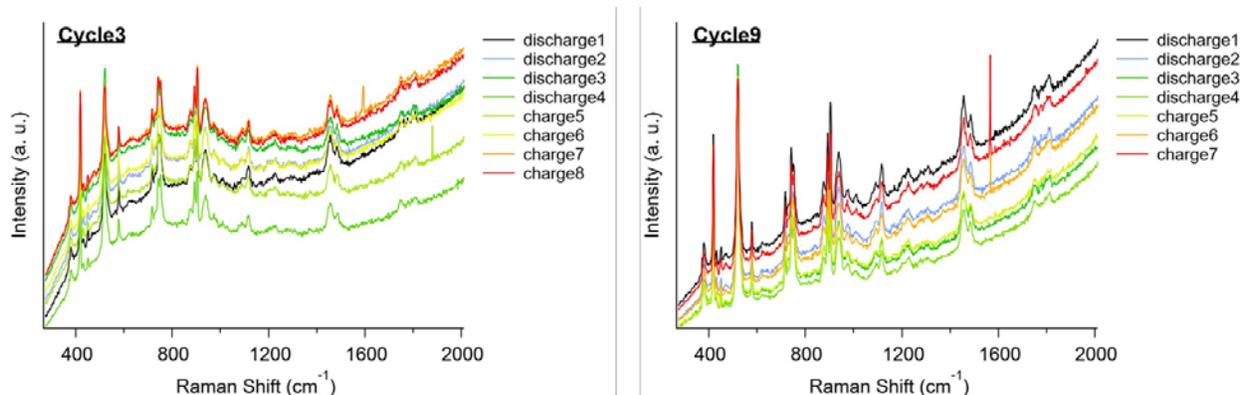
Figure 4. *In-situ* Raman spectra for the 3rd and 9th cycles.

Problems Encountered and Mitigating Strategies. Although we successfully addressed the sample damage issue by defocusing the laser beam, we still could not observe any new peaks resulting from the newly formed SEI components even after the 9th cycle. One possible explanation for this is that the reaction is occurring preferentially at the back side of the wafer, instead of at the edge and/or the front side of the wafer where the laser beam is located. Apparently, the back side of the cycled Si wafer shows a dark region where the wafer is in contact with the separator, while the front side seems to remain pristine (Fig. 5a). Such behavior can occur because the separator beneath the Si wafer is soaked with a relatively significant amount of electrolyte, allowing more facile reactions compared with the front side where relatively less electrolyte may exist between the Si wafer and sapphire window. To enhance the (electro)chemical reactions to occur at the front side of a Si wafer, we plan to coat the back side of the Si wafer with a nonconductive, inert material to prevent or alleviate any possible reactions.

Another possible explanation for observing no new peak is that the new peaks may not be visible due to the poor signal-to-noise (S/N) ratio and the fluorescent background. One possible approach is to change the laser wavelength from 532 to 633 nm. Figure 5b shows that much less background is observed with a 633-nm (red) laser compared to a 532-nm (green) laser. Although the peak intensities also decrease when the 633-nm laser is used, the S/N ratio may be better than the 532-nm laser, and there may be a better chance of observing new peaks.

Figure 3. (a) *In-situ* cell configuration and the cycled Si wafer. (b) Raman spectra collected with 532-nm vs. 633-nm lasers.

II. Influence of Water Concentration in the Electrolyte on SEI Thickness and Composition

Cell and Instrumentation Details. For the water concentration effect study, we are using a custom three-electrode O-ring cell (Fig. 6) designed and built at NREL. The base cell part accommodates a ½″×½″ Si wafer with an O-ring on top of the electrode, which enables only the area inside the O-ring (0.71 cm^2) to be exposed and reacted with an electrolyte. The O-ring is compressed by the electrolyte bath filled with 1.2 mL of Gen2 electrolyte. The additional O-ring in the bath is compressed by the top cell part that holds both lithium metal counter and reference electrodes. A separator is not used for this cell. All cells and samples were dried in a vacuum oven at 100°C overnight prior to use. All Si wafer samples were cleaned in the clean room

Figure 4. Custom O-ring cell design.

followed by the RCA (Radio Corporation of America) cleaning steps. The amount of water in the Gen2 electrolyte was controlled using a micro-syringe and confirmed using a Karl Fischer titrator. The electrolytes were used immediately after the addition of water.

Electrochemical Behavior upon Addition of Water. Based on previous studies,[2-3] we started electrochemical behavior analysis experiments with 1,000 ppm of water in the electrolyte. The Si wafers (1.7–2.3-nm native oxide layer on the surface, 675 µm, 0.01–0.02 or 0.001–0.005 Ω cm, p-type) were used as the working electrode, and lithium metal foils were used as reference and counter electrodes. For galvanostatic cycling measurements, current density of 20 µA/cm^2 was applied to the cell for 20 cycles (assigned maximum of 2 hour for a half-cycle) with a voltage range of 0.01–1.50 V as shown in Fig. 7a. While the cell with a Gen2 electrolyte showed a typical Si wafer cycling behavior, the other cell with 1,000 ppm of water was not cycled normally (may not be lithiated), possibly due to the formation of a thick non-conductive passivation layer and/or excessive side reactions with water. We could observe that the cycled electrode with 1,000 ppm of water had a white passivation layer formed at the surface of the Si wafer resulting from the reduction of the electrolyte—in particular, water—and parasitic reactions (Fig. 7a). To further study this behavior, we measured cyclic voltammogram at 1 mV/s scan rate. Figure 7b shows a large reductive current starting at around 0.9 V for the cell that included 1,000 ppm of water in both the 1st (solid line) and 10th (dotted line) cycles. This may coincide with the initial voltage spike in the galvanostatic cycling voltage profile in the presence of water. The cell voltage could not reach 0.1 V even at higher current density (30 µA/cm^2) for 20 cycles, and it showed possible Li deposition reactions at 50 µA/cm^2 (Fig. 7c).
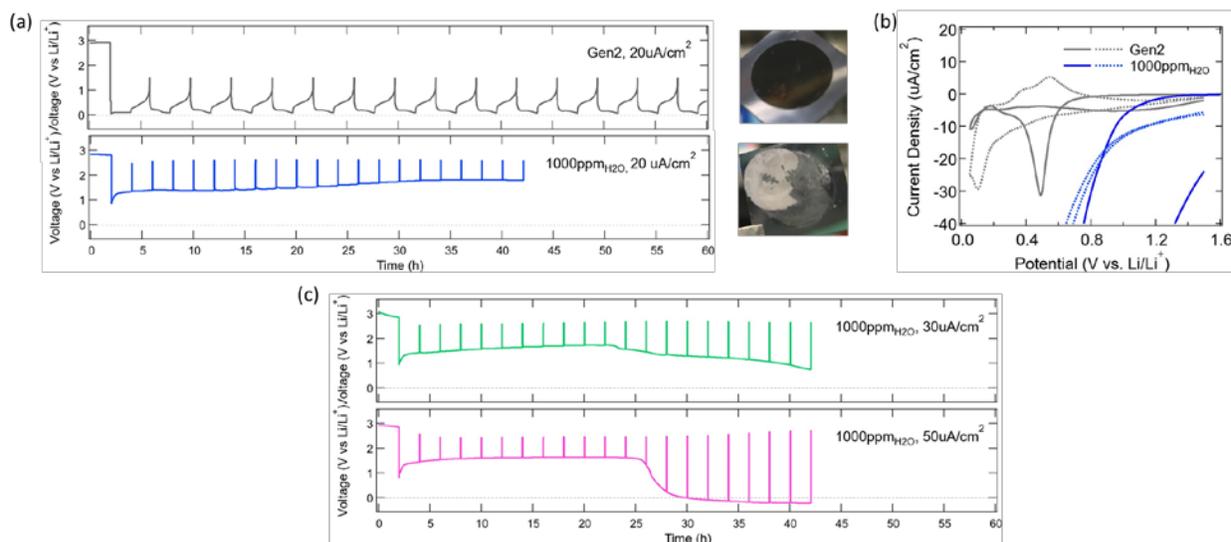
Figure 5. (a) Galvanostatic cycling without (gray) and with (blue) 1,000 ppm of water (at 20 µA/cm^2), and the corresponding images of cycled electrodes. (b) Cyclic voltammetry (scan rate = 1 mV/s) without and with water (solid lines: 1st cycle; dotted lines: 10th cycle). (c) Galvanostatic cycling with water (1,000 ppm) at 30 µA/cm^2 (green) and 50 µA/cm^2 (magenta).
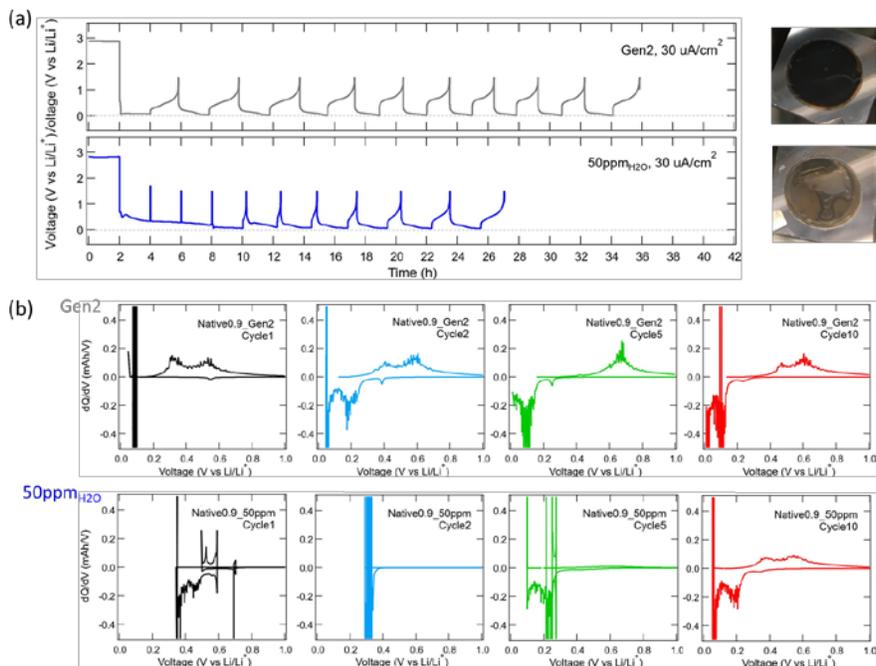
Figure 6. (a) Galvanostatic cycling without (gray) and with (blue) 50 ppm of water (at 30 µA/cm²), and the corresponding images of cycled electrodes. (b) dQ/dV plots without and with water (50 ppm) obtained from the voltage profiles in (a).

We concluded that the cells cannot be cycled with 1,000 ppm of water in the electrolyte; thus, we decided to decrease the water content to 50 ppm based on a number of cycling experiments with varying water concentrations. In addition, we increased the current density from 20 µA/cm² to 30 µA/cm² to ensure that lithiation can occur. The voltage profiles of Si wafers (0.9-nm native oxide layer on the surface, 675 µm, 0.001–0.005 Ω cm, p-type) cycled in the Gen2 $vs.$ Gen2 + 50 ppm$_{H2O}$ electrolytes are shown in Fig. 8a. The cell suffered from side reactions in the first couple cycles with Gen2 + 50 ppm$_{H2O}$ electrolyte, but the Si wafer eventually started to be lithiated. Looking at the dQ/dV plots derived from voltage profiles (Fig. 8b, with Gen2 + 50 ppm$_{H2O}$ electrolyte), we observed a number of reduction peaks at around 0.6–0.35 V for the 1st cycle and at around 0.3–0.1 V for the 5th cycle, respectively. Considering reduction behaviors of those two electrolytes, we will conduct potentiostatic experiments (voltage hold for 10 h) at 1.0, 0.5, 0.2, and 0.01 V. Another interesting feature is that the dQ/dV plot of the 10th cycle with Gen2 + 50 ppm$_{H2O}$ electrolyte almost resembles that of the 2nd cycle with Gen2 electrolyte. This indicates that the initially formed SEI layers (with water) may be dissolved into the electrolyte and/or detached from Si wafer surface, and the subsequently formed SEI layer may not be affected by the water that may be completely consumed during the initial cycles.

Characterization of Cycled Electrodes with/without Water. During the upcoming quarter, we plan to carry out several characterization experiments to better understand the effect of water contamination in electrolyte. Initially, we will transfer samples to a scanning probe microscope (SPM) mounted in an argon-filled glove box. Atomic force microscopy (AFM) will be used to measure the surface morphology of the SEIs; prior work investigating SEI corrosion/dissolution has identified the characteristic morphology of SEI after surface corrosion. In addition to analyzing nanoscale surface morphology, roughness will be measured over larger scan areas to understand the development of surface roughness on the samples. Scanning spreading resistance microscopy (SSRM) will also be employed to generate resistivity $vs.$ depth profiles for the SEIs and determine their thicknesses. The relative differences in electronic resistivity for the studied SEIs will be compared to chemical characterization obtained with X-ray photoelectron spectroscopy (XPS) to understand the composition of these interphases, present and absent water contamination.

III. Nature of the Soluble SEI Components during Cycling – Headspace Solid-Phase Microextraction GC-MS

Headspace Solid-Phase Microextraction GC-MS. Lithium salts, such as lithium hexafluorophosphate ($LiPF_6$), are known to be destructive to the gas chromatography column; therefore, direct liquid injection of Gen2 electrolyte samples should be avoided. We are developing methods for extracting molecular species present in the electrolyte (e.g., electrolyte solvents, degradation species, soluble SEI components) without the uptake of the potentially hazardous $LiPF_6$ salt. Recently, we have employed the technique of headspace solid-phase microextraction (HS-SPME), which has already been shown to work for electrolyte analysis of aged commercial Li-ion batteries (Fig. 9).[4,5] In HS-SPME, volatiles present in the headspace of a vial are diffused from the sample to the headspace, where they are adsorbed onto a polymer-coated fiber with high affinity for the target compounds. The fiber is then transferred to the injection port of the GC column, where the volatiles are desorbed for analysis.

In the experiment, an 85-μm polyacrylate fiber (Supelco) was used for HS-SPME. Headspace extraction time was 10 min at room temperature. Sample analysis was performed by manual injection into an Agilent 7890B gas chromatograph coupled to an Agilent 5977B single-quadrupole mass-selective detector. We used a split ratio of 100:1 and the temperature profile for the GC was adapted from Reference 5. Molecular species were determined by searching the mass spectra within a NIST database (MassHunter software).
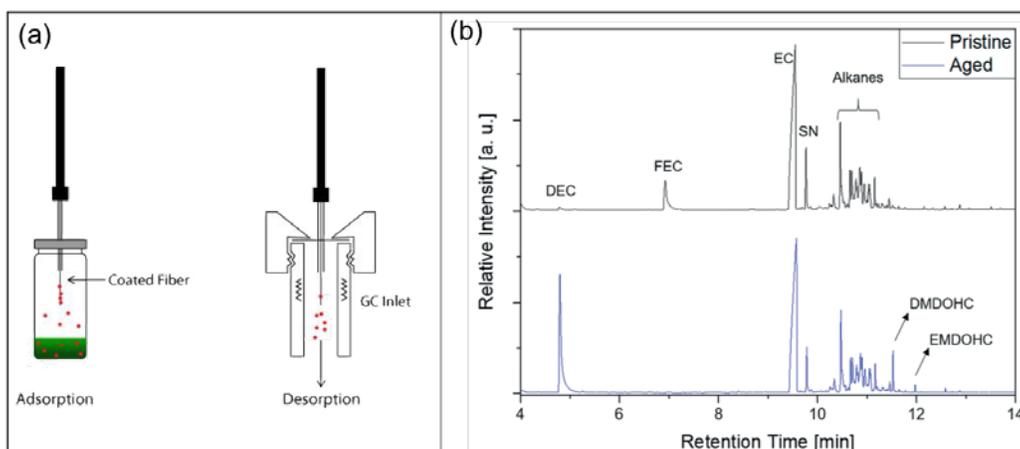
Figure 9. (a) HS-SPME GC-MS prevents injection of $LiPF_6$ salt into the GC, while still providing detection of electrolyte solvents, decomposition products and soluble SEI components.[4] (b) Horsthemke *et al.* have shown that HS-SPME GC-MS can be used to analyze electrolyte degradation products in aged commercial Li-ion batteries.[5]

Electrochemical Cycling and HS-SPME GC-MS Results. For our initial HS-SPME GC-MS study, we used about 6.5×6.5 mm^2 pieces of monocrystalline silicon wafer (675-μm thickness; boron-doped, 0.005 Ω cm) as the working electrodes. The counter/reference electrodes were Li metal foils. Celgard 2325 and Whatman GF/F glass microfiber were used for the separators, and 30 μL of Gen2 electrolyte was used. Half of the samples were rested at OCV. After an initial 2 hours rest at OCV, the others were galvanostatically cycled with an applied current of 30 μA/cm^2 between voltage limits of 0.1 and 1.5 V, and 2-hour half-cycle time limits (Fig. 10a). After 10 cycles (with charged states), all cells were carefully disassembled. The separators were placed in 10-mL glass vials, and then caps with PTFE septa were crimped onto the vials to seal them for subsequent HS-SPME.

Figure 10b shows the gas chromatographs of the cycled cell *vs.* one left at OCV. For comparison, we also used the same SPME method to sample the headspace above a vial containing 200 μL of only Gen2 electrolyte. All

three samples yield similar results: a large EMC signal at a retention time around 4.1 min, a large EC signal around 12.3 min, and a smaller DEC signal around 6.4 min. The presence of DEC is not surprising because it is a known byproduct of EC reduction in the presence of EMC. The inset of Fig. 10b shows a zoom-in of the chromatographs between 10 and 14 mins. Some small differences are apparent between the samples, but the signal intensities are too low for us to confidently identify them at this time.
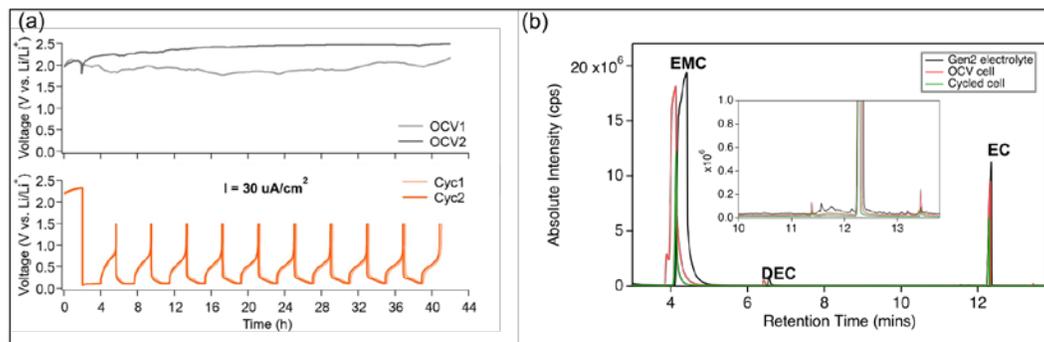
Figure 10. (a) Electrochemical performance of coin-type cells (with Si wafer *vs.* Li metal): Half of the samples were rested at OCV, whereas the other half were galvanostatically cycled between 0.1 and 1.5 V at an applied current of 30 μA/cm². (b) Gas chromatograms using HS-SPME to sample the headspace above the separators (red and green lines) and pristine Gen2 electrolyte for comparison (black line); [inset: zoom-in at retention times between 10 and 14 minutes].

Conclusions

Based on an additional literature survey and Raman measurements with neat solvent(s) and/or electrolytes, we have refined the reference table for Raman peak assignments. In addition, we successfully addressed the sample damage issue by defocusing the laser beam, but we still could not observe any new peaks induced from the newly formed SEI components. We plan to 1) coat the back side of the Si wafer with a nonconductive and inert material to prevent any possible reactions of the back side and enhance the (electro)chemical reactions occurring at the front side of a Si wafer, and 2) change the laser wavelength from 532 to 633 nm to minimize fluorescence interference, thus enabling one to observe new peaks.

Because of the reduction behaviors of two electrolytes (i.e., Gen2 *vs.* Gen2 + 50 ppm$_{H2O}$), we plan to conduct potentiostatic experiments (voltage hold for 10 hours) at 1.0 V, 0.5 V, 0.2 V, and 0.01 V. All controlled samples will be characterized using a variety of analytical techniques including XPS, AFM/SPM/SSRM, TOF-SIMS, Raman/FT-IR, and STEM to understand the underlying chemistry and physics and provide a mechanical explanation of surface chemistry and various reactions/interactions within the SEI.

The idea to detect soluble SEI components with HS-SPME GC-MS remains promising, but we believe that improvements are needed in our experimental design. First, we plan to modify the x-wing cell to require much less electrolyte. Having greater than 2 mL probably dilutes the sample too much, despite the high sensitivity of GC-MS. Although a preliminary study with unoptimized conditions, we have shown here that it is possible to analyze the volatile molecular components present in the electrolyte after cell cycling. Moving forward, we must refine both the HS-SPME (time and temperature) and the GC (split ratio and heating) parameters to minimize the overwhelming EMC and EC solvent signals, but still detect soluble SEI species. In future studies, we plan to 1) investigate how adding small amounts of water to the electrolyte might yield more soluble SEI components (e.g., via HF etching of the anode surface after HF formation from hydrolysis of LiPF$_6$) and 2) build upon recent efforts studying early-stage SEI formation using pre-lithiation voltage cutoffs.

References

1. G. Gachot *et al.*, *Analytical Chemistry* **2011**, *83*, 478–485.
2. D.J. Xiong *et al.*, *J. Electrochem. Soc.* **2016,** *163* (8), A1678–A1685.
3. R. Bernhard *et al.*, *J. Electrochem. Soc.* **2015,** *162* (10), A1984–A1989.
4. http://2014.igem.org/Team:Valencia_UPV/Project/modules/methodology/sample_preparation.
5. F. Horsthemke *et al.*, *RSC Advances* **2017,** *7* (74), 46989–46998.

Silicon/Electrolyte Interface Stabilization (NREL)

Ivana Hasa, Elisabetta Arca, Glenn Teeter (PI), Robert Kostecki (PI) (NREL)

Background

Two sets of samples were prepared at Lawrence Berkeley National Laboratory (LBNL) to study solid-electrolyte interphase (SEI) formation and evolution during cycling of thin-film Si-based anodes with varying thicknesses of SiO_x. Thin-film (50 nm) amorphous silicon (a-Si) was sputter deposited on Cu-foil current collectors. In one set of samples, native oxide (estimated ~3 nm thick) was allowed to form on the surface of the anode. In the second sample set, a 10-nm-thick SiO_x layer was sputter deposited on the a-Si layer. Galvanostatic cycling was performed by applying a constant current of 5 mA cm^{-2} within the 0.05–1.5 V potential range in a three-electrode Swagelok T-type cell, using Gen 2 electrolyte (1.2M LiPF$_6$, EC:EMC 3:7 wt.%). Following galvanostatic testing, samples were rinsed with DEC, packaged, and shipped to the National Renewable Energy Laboratory (NREL) for X-ray photoelectron spectroscopy (XPS) measurements. At NREL, samples were transferred from an argon-filled glovebox into the XPS analysis chamber via an ultrahigh-vacuum transport pod to avoid exposure to ambient atmosphere. XPS measurements were performed in a Kratos Axis Nova instrument.

Results

XPS measurements on the 50-nm a-Si / 3-nm SiO_x sample are summarized in Fig. 1. Initially, during the first lithiation (1.5 V), XPS spectra primarily showed the presence of SiO_x (Si 2p and O 1s peaks at ~105 eV and 534.2 eV, respectively), as well as the underlying Si^0 (Si 2p peak at ~99.5 eV). Additionally, there appears to be a small amount of Li_ySiO_x present even at 1.5 V. As the first lithiation proceeds down to 0.05 V, the most striking changes include the appearance and growth of peaks associated with $(CO_3)^{2-}$, LiF, and a P-F-containing species. Possibly the $(CO_3)^{2-}$ functional group exists in the SEI in the form of Li_2CO_3. The P-F species is revealed by F 1s and P 2p peaks (~690.5 eV and ~138 eV, respectively) that are strongly correlated with respect to both relative binding energies (BEs) and peak intensities. The existence of $(PF_6)^-$ (or $LiPF_6$) as a candidate to explain the observed P-F features is tentatively ruled out because the observed F 1s to P 2p BE values (~553 eV) do not match the expected value for $LiPF_6$ (~552 eV). Also, the observed peak intensity ratios F/P are too low to be consistent with $(PF_6)^-$; therefore, we speculate that these peaks are associated either with relatively F-deficient Li_xPF_y phases [1], or possibly POF_3 or PF_3. Further measurements are planned, including on $LiPF_6$ reference samples, to more definitively identify the P-F-containing species.

XPS measurements for the 10-nm SiO_x samples are shown in Fig. 2. For the most part, the same phases are observed for the SEI in these samples as were seen in the native-oxide samples. On the other hand, significantly less $(CO_3)^{2-}$ is seen for the 10-nm samples than for the native-oxide sample, and it forms at substantially lower potentials. Also, fewer Li_ySiO_x phases are observed for the 10-nm sample. In contrast to the native-oxide samples, relatively more LiF and P-F-containing phases form on the 10-nm samples, especially at the lowest lithiation potential (0.05 V).
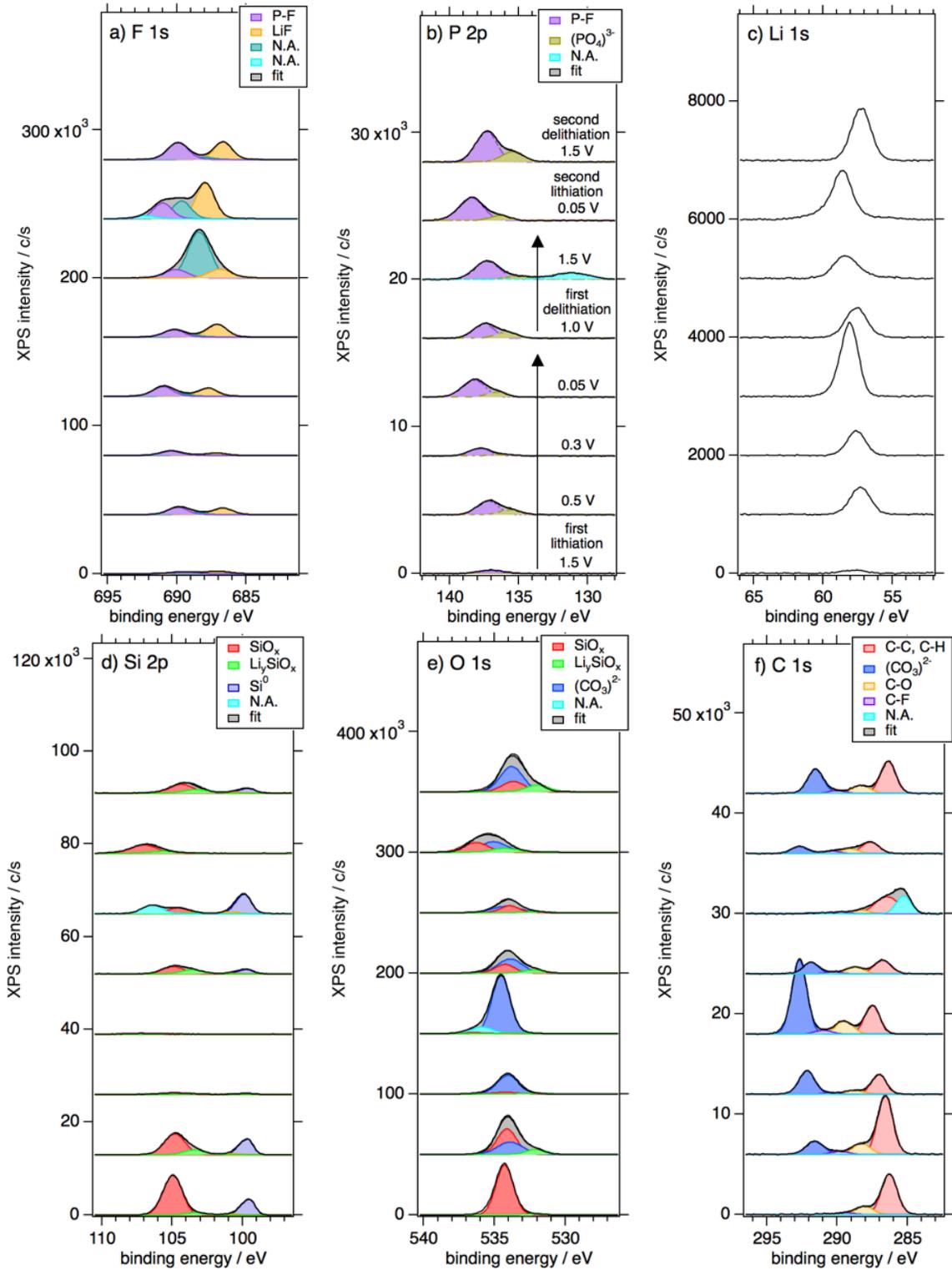
Figure 1. Summary of XPS measurements on 50-nm a-Si / 3-nm SiO₂ films at varying states of lithiation and delithiation. Peak assignments are preliminary, N.A. denotes "not assigned."
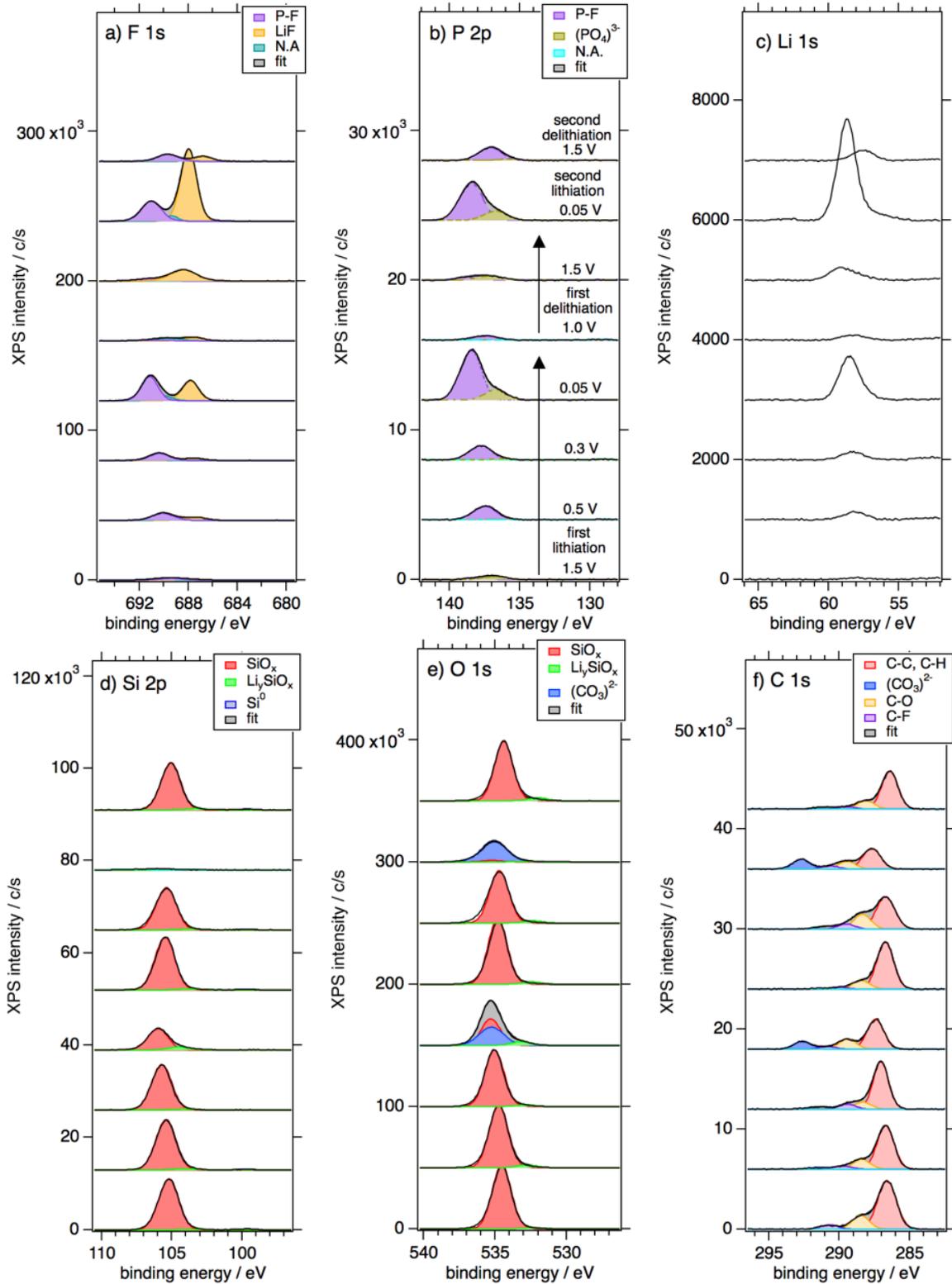
Figure 2. Summary of XPS measurements on 50-nm a-Si / 10-nm SiO$_2$ films at varying states of lithiation and delithiation. Peak assignments are preliminary, N.A. denotes "not assigned."

An interesting feature for both the native-oxide and 10-nm SiO_x samples is that the peaks associated with $(CO_3)^{2-}$ are most intense at the lowest lithiation potentials (0.05 V) and subsequently decrease during delithiation. Similar effects are seen with both LiF and the P-F-containing phase. Furthermore, the attenuation of Si^0 and SiO_x XPS signals also indicates that SEI layer thickness tends to increase during lithiation and decreases during delithiation. These observations suggest that formation of these phases is partially reversible, or that after formation these phases can detach from the SEI. Another possibility is that these phases are poorly adhered within the SEI and are washed away during the DEC rinse applied during sample preparation.

C 1s spectral features tentatively assigned to C-C, C-H, C-O, and C-F moieties are observed on all samples, and, in general, the magnitudes of these peaks are not strongly correlated with lithiation/delithiation potential. With the exception of Si^0 peaks, there is considerable variability in measured BE values for all phases, indicating varying degrees of charging during the XPS measurements. For both the native-oxide and 10-nm SiO_x samples, the observed trend is that peaks shift to higher BEs at lower lithiation potentials, which is consistent with lower net ionic and electronic conductivities in these SEI layers.

Conclusions

XPS measurements were performed on a-Si / 3-nm SiO_x and a-Si / 10-nm SiO_x films deposited on Cu-foil current collectors. Key results of the XPS analysis include the following:

- For the native-oxide samples, a substantial fraction of the initial SiO_x layer is converted to Li_ySiO_x phases during the first two cycles, but very little Li_ySiO_x is seen in the 10-nm SiO_x samples.

- Phases and moieties including LiF, $(CO_3)^{2-}$, $(PO_4)^{3-}$, and P-F are clearly observed.

- The relative phase composition of the SEI layers evolves significantly over the course of cycling.

- SEI phase evolution in the 10-nm samples primarily occurs at markedly lower potentials than observed in the native-oxide case.

References

1. L. Martin, H. Martinez, D. Poinot, B. Pecquenard, F. Le Cras, *Journal of Power Sources* **248**, 861–873 (2014).

Silicon Electrolyte Interface Stabilization (SEISta)

Josey McBrayer (SNL), Chris Apblett (SNL), Eric Allcorn (SNL)

Background

This quarter, we focused on preparing to measure elastic and loss modulus of grown and amorphous SiO_2 films as Li enters the film (the Q3 milestone), depending on temperature and C rate. We had originally thought to use atomic force microscopy to do this work, but that tool is no longer available for Si anode work at Sandia. So we modified the work on the stress measurement to include this work and to measure modulus and strain evolution on the lithiation of the grown SiO_2 films, starting with thin-film Si.

Results

Strain in growing SEI films. This quarter, the moiré microscope mentioned in the Q2 report was completed and thermal expansion experiments were performed to verify the microscope's functionality and applicability for measuring strain in silicon and the SEI in the future. A film of 500 nm of Cu was evaporated on a silicon wafer. A grating, with a period of 4 µm, was then patterned on top of the Cu. The amplitude grating consisted of 2-µm bars of 610-Å-thick Si. With an incident light wavelength of 470 nm, the silicon has near-zero reflectance while the copper has near-total reflectance. Moiré fringes that are formed due to the offset of the sample and reference gratings (Fig. 1A) create a sine wave with varying amplitude (shown in Fig. 1B). The frequency of this sine wave is consistent over the area of interest, indicating uniform heating of the sample. By fitting the sine wave and tracking the change in frequency with temperature, the strain and coefficient of thermal expansion (CTE) of the material can be determined. The silicon wafer substrate has a theoretical CTE of about 3–5×10^{-6} 1/K in the temperature range studied.[1] As seen in Fig. 1C, the experimental CTE can be found from the slope and is estimated as 4 ± 0.9×10^{-6} 1/K. Each 30°C change in temperature corresponds to ~0.0001 change in strain whereas the lower limit of strain measured in silicon anodes in the literature is on the order of 0.003.[2-4] This demonstrates the nondestructive ability of moiré microscopy to measure the strain in silicon and the presumably smaller changes in strain caused by the formation of the SEI. Next, we will apply this confirmed technique to the *in-situ* measurement of strain during the operation of a battery.
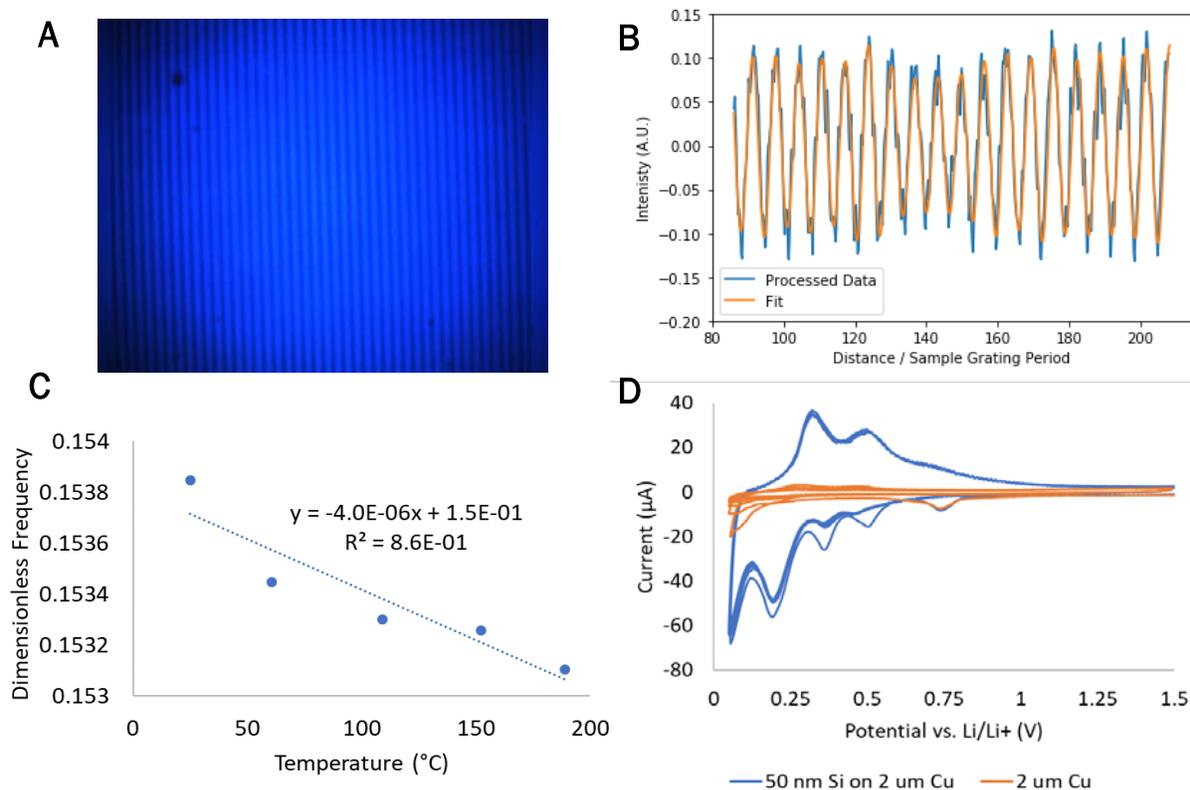
Figure 7. A) Moiré fringe pattern using 470-nm incident light for the Si wafer thermal expansion experiments, B) Cross-sectional average of the moiré fringe pattern given in A with the data in blue and the fit in orange, C) Dimensionless frequency obtained from the sine-wave fit for each temperature, with the slope giving the CTE of the silicon wafer substrate, and D) Cyclic voltammogram of the 50-nm Si on 2-µm Cu in blue and 2-µm Cu in orange. Contamination peaks seem to be present during the first cycle.

A specially designed *in-situ* cell and foil electrode are necessary to perform *in-situ* moiré microscopy. The *in-situ* cell must provide backside access to the sample grating on the foil. The prototype described in the Q2 report has been improved and newly manufactured. A novel technique has been employed to create Si-on-Cu foils as model electrodes. Photoresist was deposited on a silicon wafer. Next, 50 nm of Si was evaporated onto the photoresist, followed by 2 µm of Cu. This enabled a smooth surface between the silicon and copper. The foils were removed from the silicon wafers and photoresist by soaking in acetone and were cleaned by rinsing with IPA and performing a brief O_2 plasma clean. The cyclic voltammograms of 2-µm Cu and 50-nm Si on 2-µm Cu are shown in Fig. 1D. In the first cycle, there are two contaminant peaks at ~0.74 V (Cu and Si samples) and 0.5 V (only Si samples) vs. Li/Li$^+$ in the first cycle that are not typically observed in the literature. Subsequent experiments are being performed to identify and remove the contaminants.

Conclusions

Progress in establishing a high-resolution, high-sensitivity strain measurement technique that also allows *in-situ* electrochemistry to occur on Si samples has been established. New sample preparations based on historical electron-beam evaporated Si on very thin (2-µm-thick) Cu substrates has been demonstrated, and the electrochemistry is in line with samples of Si cycling in Gen-2 electrolyte—with one noticeable difference on a first lithiation peak at ~0.74V vs. Li, which has not been previously observed. We are conducting experiments to determine why this peak exists. But it exists on both bulk Si and our thin-film Si, so it is possible that it is either a contaminant from the cleaning process (HF is used as the last step against the standard SEISta protocol) or is due to contamination in the electrolyte or the Li. Measurements as small as ~2 nm of deflection

from the strain in these samples has been measured, so the sensitivity of the optical technique has been established.

In-Situ Formation of Li-Mg-Si Zintl Phases to Stabilize Silicon Anodes

Baris Key, Binghong Han, Fulya Dogan, Chen Liao, Steven Trask, Saul Lapidus, Jack Vaughey (ANL)

Background

The overall reactivity of lithium silicide (LS) Zintl phases that form upon lithiation of silicon greatly affects the formation and stability of the solid-electrolyte interphase (SEI) and has been shown to reduce the efficiency of the Li-Si system. It is essential to control this reactivity by tuning the chemistry to achieve a stable high-efficiency silicon anode electrochemistry.

Results

Previously, researchers have found that substituting Mg, Zn, and Al into a lithium-rich LS Zintl phase will significantly improve its thermodynamic stability.[1,2] However, the affect of metal substitutions on the chemical stability of these reduced compounds in contact with electrolytes has not been reported. In this study, we first used the synthesized crystalline magnesiated LS (MLS) and LS as model compounds of the charged silicon electrodes to investigate whether the substitution of other metal cations into the lithiated Si could reduce its deleterious interactions with the electrolyte solvents. The scanning electron microscopy (SEM) images and X-ray diffraction (XRD) patterns of the pristine LS and MLS model compounds are shown in Fig. 1, which have the target stoichiometry of Li_7Si_3 and Li_2MgSi, respectively. The XRD pattern of the pristine LS powders in Fig. 1a shows that the LS powder also contains $Li_{12}Si_7$, a slightly more silicon-rich phase in the system that results from high-temperature lithium evaporation. Similarly, for the pristine MLS powders, the XRD pattern in Fig. 1b shows Li_2MgSi and a small amount of Li_8MgSi_6 phases. Although the actual lithiated species formed during the charging of Si anodes could be amorphous,[3] previous solid-state nuclear magnetic resonanace (NMR) studies have shown that the local Li chemical environment in amorphous LS is comparable to those in the crystalline LS.[4-6] Therefore, the LS and MLS model compounds synthesized in this work were used as a model system to simulate the potential interactions between electrolyte solvents and lithiated Si anodes. It is worth noting that the freshly synthesized LS powders are found to be surprisingly reactive after being packed and spun in ZrO_2 NMR rotors despite the large particle size observed by SEM; the section of ZrO_2, a geologically stable oxide in direct contact with the fresh powders, blackened after an overnight experiment (see Fig. 1a). Staying in the ZrO_2 rotor for a longer time caused the delithiation of pristine LS and finally the formation of a diamagnetic Li phase. A similar phenomenon was not observed for powders aged in an Ar glovebox after several weeks. In comparison, the rotor in contact with fresh MLS powders did not undergo any discoloration after an overnight experiment (see Fig. 1b). Considering the reactivity of LS and MLS model compounds, the reactivity experiments done in this study were all measured immediately after mixing the pristine LS or MLS powder with different electrolyte solvents, analogous to electrochemically generated Zintl phases being constantly exposed to electrolyte solvents in a battery due to volume changes.
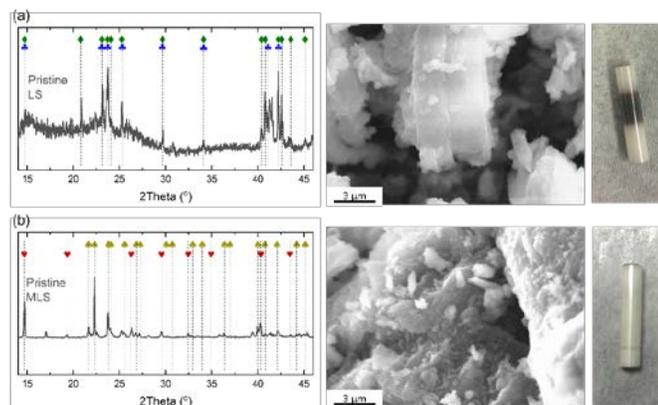
Figure 1. XRD results and SEM images of pristine (a) LS and (b) MLS powders, as well as the photos of NMR rotors in contact with the pristine LS and MLS powders after 24 h. The XRD reference peak positions marked by blue clubs and green diamonds in panel (a) represent the Li_7Si_3 and $Li_{12}Si_7$ phases,[5] respectively. The XRD reference peak positions

marked by red hearts and yellow spades in panel (b) represent the Li_2MgSi and Li_8MgSi_6 phases, respectively.[7, 8] The rotors in the photos were made of ZrO_2 and were initially colorless. The blackish part in the center of the ZrO_2 tube is the region directly in contact with LS powders during NMR measurement, whereas the white parts on two ends are the regions with no contact.

To investigate the *in-situ* reactions of model compounds in contact with different common electrolyte solvents, pristine LS and MLS powders were mixed with EC and EMC, respectively, with the volume ratio of 1:1, followed by NMR measurements. EC is in solid form at room temperature, so the mixture of EC and LS powders were first heated to 325 K inside the NMR probe to let the EC melt and encompass the LS and MLS powders and then cooled back to room temperature for NMR measurements. Figures 2a and 2b show the ^{7}Li and ^{29}Si MAS NMR results of the mixture of LS with EMC and EC. Compared with the pristine LS, the mixture of LS and EC shows a positive chemical shift of 2.4 ppm in ^{7}Li NMR, and a significant change in ^{29}Si NMR, which suggests loss of Li^+ from the LS compounds based on literature reports.[5] In comparison, the chemical shifts in ^{7}Li and ^{29}Si NMR after mixing LS with EMC are only 0.7 and 1.9 ppm, implying that EMC can be considerably less reactive in contact with LS and can cause less Li loss compared with EC. The biphasic nature of the synthesized MLS likely introduces a lineshape complexity in Figs. 2c and 2d as well as the fact that Li-Mg-Si phases resonate at higher frequencies. In addition, we also tested the reactivity of LS with Gen2 electrolyte, which contains both EC and EMC, and the ^{7}Li NMR result shows that mixing LS with Gen2 electrolyte leads to peak shifts similar to the EC case (data not shown). After washing the LS+Gen2 mixture with DMC, the ^{13}C and ^{1}H NMR results showed (data not shown) the presence of insoluble carbonates. Based on the changes in ^{7}Li NMR results in Fig. 2a and the deshielding observed in ^{29}Si resonance in Fig. 2b, the reactions shown in Scheme 1 is proposed: that silicon anions in LS initiate the reaction to lose electrons (and Li, not shown), reducing and decomposing EC and EMC to produce organic lithiated carbonates with or without gas generation (e.g., LiEDC or LiEC/LiBDC, respectively). The reaction of EC with silicon anions was more pronounced spectroscopically, likely due to the prevalence of ring-opening reactions. The results from the LS model compound are consistent with previously reported reaction mechanisms.[9] On the other hand, the ^{7}Li NMR results in Fig. 2c show that mixing MLS with EC only leads to a small peak shifts of ~0.3 ppm compared with the pristine MLS, which are much smaller than the peak shifts after mixing LS with EC in Fig. 2a. Similarly, the ^{29}Si NMR shifts after mixing MLS with EC (Fig. 2d) are also much smaller than that after mixing LS with EC (Fig. 2b). The peak shifts in ^{7}Li and ^{29}Si NMR after mixing MLS with EMC is even smaller. The above results imply that substituting Mg into the LS lattice can effectively stabilize the lithiated silicides against electrolyte solvents. It must be noted that the compositions studied here cannot be generalized to the electrochemically formed domains of highly reduced silicon anions; therefore, these results are not meant to be a predictor for complete stability. The goal of our model-compound study is to modulate the instability of the anions with or without Mg doping.
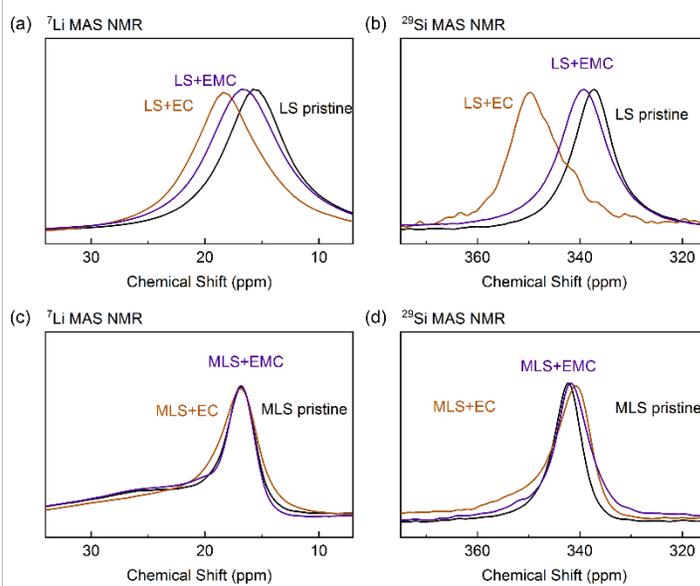
$$[Si\text{-}Si]^{-4} \longrightarrow 2[Si]^{-2}$$

$$[Si]^{-2} \longrightarrow 2\,\delta e^- + [Si]_2^{2\delta-2}$$

$$2 \quad \underset{O}{\overset{O}{\bigcirc}}\!\!O \quad \xrightarrow{2\,e^-} \quad 2 \quad \ominus O \overset{O}{\underset{}{\bigcirc}} O\text{-}Et\,.$$
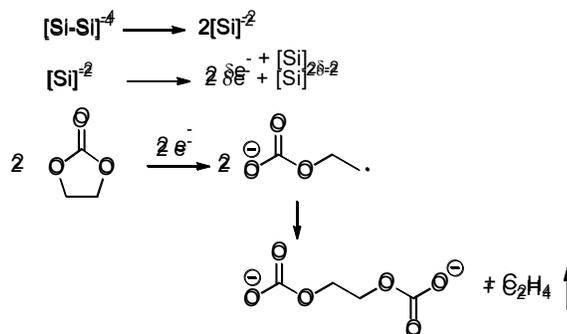
Scheme 1. Proposed reactions based on characterization results

Table 1. Formulations and notations of the electrolytes used in this study

Notations	Components
Gen2	1.2 M LiPF$_6$ in 30 wt% EC + 70 wt% EMC
GenF	Gen2 electrolyte + 10 wt% FEC
GenFM	GenF electrolyte + 0.1 M Mg(TFSI)$_2$

Encouraged by the model compound chemical stability, we report for the first time the use of Mg and other metal salts as electrolyte additives to stabilize the cycling of Si electrodes. The central idea is the co-insertion of Mg and Li cations into Si electrode during the lithiation process, forming less-reactive metal-substituted LS species in an *in-situ* fashion and reducing the reactivity of charged Si anodes. 0.1 M Mg(TFSI)$_2$ was added into the baseline GenF electrolytes to formulate the new GenFM electrolyte (see Table 1 for the formula and acronyms of all electrolytes used in this study). The half-cell results on Si electrodes fabricated by Argonne's Cell Analysis, Modeling and Prototyping (CAMP) Facility are shown in Fig. 3. For the baseline GenF electrolyte with no Mg salt, the half-cell delithiation capacities start at ~2600 mAh/g$_{Si}$ and quickly drop to ~2000 mAh/g$_{Si}$ after three formation cycles at C/20. Then, during the 20 fast C/3 cycles, the capacities decrease from ~1500 to ~200 mAh/g$_{Si}$ with the Coulombic efficiencies dropping from ~96% to ~92%. In comparison, in GenFM electrolyte containing 0.1 M Mg(TFSI)$_2$, the delithiation capacities start from ~2800 mAh/g$_{Si}$ in the first cycle and are as high as 2650 mAh/g$_{Si}$ even after three formation cycles at C/20. During the 20 fast C/3 cycles, the capacities decrease from ~2200 to ~1650 mAh/g$_{Si}$ and the Coulombic efficiencies are maintained at ~97%, which are much better than the baseline GenF electrolyte performance. The capacity drop in GenFM electrolyte from C/20 formation cycles to C/3 aging cycles is likely caused by a rise in cell impedance. If low-cutoff voltage holds at 0.01 V until C/200 is reached at the end of lithiation process are applied—not only during the formation cycles but also during the fast aging cycles—then a remarkably stable delithiation capacity of ~ 2550 mAh/g$_{Si}$ with Coulombic efficiencies ~98.5% can be obtained with the GenFM electrolyte (Fig. 4) for 10–0 cycles until plating starts. In addition, the GenFM half-cell shows a faster current fading and stabilization than the GenF cell (see Fig. 4c) during potentiostatic holds at 10 mV in the first delithiation process, indicating that GenFM electrolyte reduces parasitic currents by an order of magnitude; this suggests that adding Mg can help to reduce the side reactions of lithiated Si electrodes with electrolytes and therefore improve the cell performance. The approximation can be done because the addition of the Mg is the only variable introduced to the system as LiTFSI and/or increased salt concentration has been found to have no effect on performance and Li-M-Si phases have been shown directly to be relatively less reactive from

the model compound study. Further *ex-situ* and *in-situ* characterization studies are needed to confirm this in detail. The dQ/dV profiles do not show any major changes in the electrochemistry between the GenFM and GenF electrolytes during the initial formation cycles (Fig. 3). When comparing the first formation cycle with the third formation cycle, in GenFM electrolyte, fewer peak shifts can be observed during both lithiation and delithiation processes compared with those in GenF electrolyte, which is consistent with the much better capacity retention observed in GenFM electrolyte. The dQ/dV profile of the half cell cycled in GenFM electrolyte is totally different from the cycling data on Mg-Si alloy anodes reported previously.[10,11] We observed almost no contribution to the dQ/dV profile from the addition of Mg salt except subtle shifts of the lithiation peak at 0.21 V (to higher voltages) and the delithiation peak at 0.42 V (to lower voltages), which are likely due to small amounts of Mg inclusion into the Zintl phase (Figs. 3c and 3d). These results suggest that adding $Mg(TFSI)_2$ as a second salt (anions other than $TFSI^-$ in principle should work just as well) is a simple and effective way to suppress the side reactions between the electrolyte and Si electrodes without diminishing the high capacity of Li-Si chemistry—and, at the same time, to increase the retention rates and efficiencies of Si anodes, which is consistent with our model-compound observations.
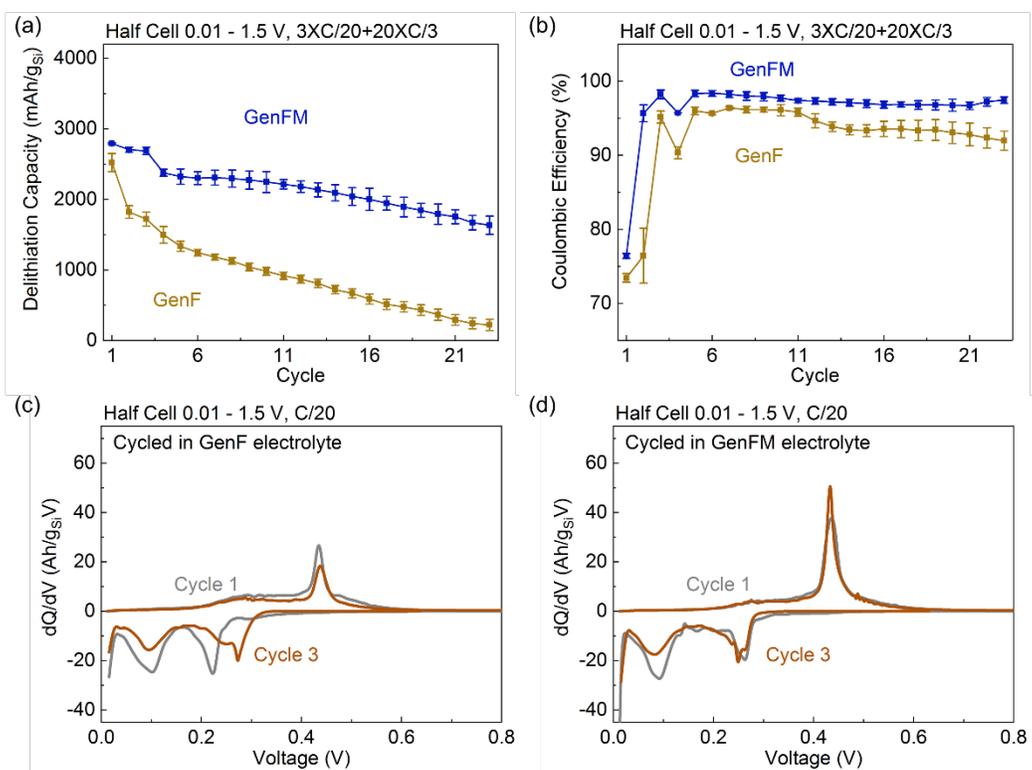
Figure 3. Half-cell electrochemical test results on Si electrodes. The GenF and GenFM electrolytes were used in the electrochemical tests. The delithiation capacities and Coulombic efficiencies are shown in panels (a) and (b), respectively. The differential capacities at the first and third formation cycles in GenF and GenFM electrolytes are shown in panels (c) and (d), respectively. The cells were cycled between 0.01 V and 1.5 V, first at the rate of C/20 for 3 formation cycles, then at the rate of C/3 for aging cycles. The capacities are normalized by the mass of silicon. Error bars represents the standard deviations of at least three measurements for each sample.
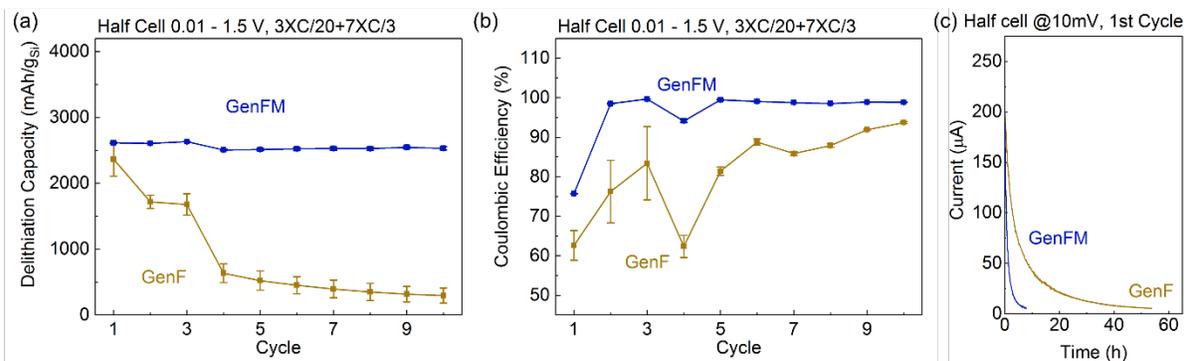
Figure 4. Half-cell electrochemical test results on Si electrodes with low-cutoff voltage holds during both formation and aging cycles. The GenF and GenFM electrolytes were used in the electrochemical tests. The delithiation capacities and Coulombic efficiencies are shown in panels (a) and (b), respectively. The capacities are normalized by the mass of silicon. The cells were cycled from 0.01 to 1.5 V, first at the rate of C/20 for 3 formation cycles, then at the rate of C/3 for aging cycles. The cells were held at 0.01 V until the current dropped below C/200 at the end of each lithiation process during both formation and aging cycles. Extensive voltage holding at 0.01 V in every cycle results in eventual lithium plating and cell death after 15+ cycles for GenFM. Error bars represent the standard deviations of at least three measurements for each sample. (c) Current change of the representative half cells with GenF and GenFM electrolytes in the first lithiation process during the voltage hold at 10 mV.

To understand whether Mg is co-inserted into the Si anodes during the lithiation process, fully lithiated electrodes were harvested to obtain the active materials from the Cu foil for further characterization experiments. The harvested electrode powders have been washed with DMC to remove the precipitated Li and Mg salts left on the surface. As shown in Fig. 5a, the Si electrode lithiated in GenFM electrolyte (containing 0.1 M $Mg(TFSI)_2$) shows distinct but broad peaks in the XRD pattern, suggesting the formation of $Li_{15-x}Mg_xSi_4$ phases (assuming a constant 15:4 ratio between cations and Si) with small-crystalline or semi-amorphous features.[1, 2] More importantly, the formation of a single $Li_{14.65}Mg_{0.35}Si_4$ phase (Mg:Si ratio of ~1:11) is confirmed by synchrotron high-resolution X-ray diffraction (HRXRD) characterization and refinement analysis shown in Fig. 5b. This is a critical observation because it directly proves Mg co-insertion in the bulk and confirms that M incorporation can generate a single-phase product electrochemically at full lithiation of silicon. The refinement shows lattice parameters of a = b = c = 10.7211 Å, close to the $Li_{13.63}Mg_{1.37}Si_4$ phase reported before (ICSD 429404, where a = b = c = 10.7418 Å). Synchrotron HRXRD also confirms the minor (042) reflection at 9.9° (see the insert in Fig. 5b) due to ternary formation that was not detected using lab X-rays due to low signal-to-noise ratio. No crystalline compound such as Mg_2Si was detected by XRD, HRXRD, or TEM (see Fig. 5e) after lithiating Si electrode in GenFM electrolyte. However, ~3% MgO was estimated from HRXRD as well as other less minor crystalline phases (evident in difference plot). The former is likely due to the reaction of $Mg(TFSI)_2$ with water impurity (in the binder and the electrolyte) and/or the silicon oxide shell present on the pristine silicon particles; the latter is due to other unconfirmed decomposition products such as MgF_2, $Mg(OH)_2$, other electrolyte reduction species, etc. The energy-dispersive X-ray spectroscopy (EDS) results of the lithiated material in Fig. 5e show that significant amounts of Mg can be found both on the surface and in the bulk of lithiated Si particles with the Mg:Si ratio of ~1:9 after the lithiation in GenFM electrolyte; this is in agreement with the HRXRD results, indicating that using Mg-containing electrolyte does allow for the co-insertion of Mg cations into the Si during the lithiation process, forming semicrystalline Li-Mg-Si ternaries below the Mg:Si concentration in $Li_{14}MgSi_4$. Meanwhile, the formation Mg-Li or Mg-Si structures are not observed during the *in-situ* Mg insertion/doping process, unlike previously reported cases where higher Mg contents were used in solid state.[11] The electrode with 1 full lithiation/delithiation cycle was also studied and its XRD pattern is shown in Fig. 5a, which did not indicate any crystalline phases. Figure 5f shows that after delithiation to 1.5 V vs. Li in GenFM electrolyte, the Mg:Si molar ratios increase on the surface and decrease in the bulk compared to the fully lithiated sample. This implies that during the delithiation process, some Mg cations have migrated from the bulk of Si to the surface

40

and/or trapped by the SEI layer. After 9 cycles in GenFM, when the Si electrode is fully lithiated again, Mg can still be found evenly distributed in the surface and bulk of the Si particles; however, the Mg:Si ratio drops down to ~1:20 (data not shown). It is interesting to note that if a different silicon batch with more crystalline Si and SiO_2 content is used (e.g., SiO_x), then although an improvement in initial capacity and capacity retention was again noted, significantly more Mg can be found on the surface regions; this is consistent with the formation and stability of MgO, with Mg being very oxophyllic.[12] The formation of MgO could insulate the surface and hinder the Li transportation processes, but it may also help to passivate the reaction between lithiated Si and electrolyte. The clear role of MgO in SEI requires further investigations in the future. Si materials from different vendors with different surface oxidation status and/or particles sizes also show various response to the adding of Mg salt. The smaller Si with less surface oxidation such as 80-nm spherical particles from HydroQuebec with only a few nm of SiO_2[13] demonstrated considerable capacity and efficiency improvement after adding Mg, whereas the larger Si with thicker surface oxidation layers (such as NanoAmor or Sigma Aldrich Si) showed even worse performance with GenFM electrolyte. Based on these results, such oxophyllic M chemistries by nature are better suited to systems where M can access Si more readily and with binder, solvent, particles, and processing methods with less water and oxide content such as SiO_2.

The Si electrodes lithiated in GenFM electrolyte were also characterized by MAS NMR. The ^7Li NMR results in Fig. 5c demonstrate the evolution of Li contents and its local environments after a different number of cycles for fully lithiated electrodes. The peak around 0 ppm is from the diamagnetic Li species mainly in the SEI layer, whereas the peaks at higher frequencies than 5 ppm represent the Li inserted into the Si. Compared with the electrochemically obtained $Li_{15+x}Si_4$ phase (marked with green dotted line at 6.7 ppm),[5] a significant shift of 4.3 ppm in the Li resonance peak of lithiated Si electrode after initial discharge (marked with black dash line at 11.1 ppm) can be observed in Fig. 5c. Such a shift of the resonance toward high frequencies is consistent with the doping of Mg cations (with more valence electrons) into the fully lithiated Si electrode. No resonance due to $Li_{14}MgSi_4$ composition was observed (previously reported at 43 ppm[1]), consistent with the previous EDS and XRD results. After 11 and 17 cycles in GenFM electrolyte, the ^7Li NMR results on the re-lithiated Si electrodes show a resonance shift to lower frequencies by -1.7 ppm, appearing at 8.6 ppm (marked with red dashed line), suggesting a decrease in Mg concentration in the Zintl phase. This is consistent with the reduction in Mg:Si ratios after cycling observed in EDS analysis. Furthermore, the ^{29}Si NMR of the lithiated GenFM sample shows a peak center around -55 ppm in Fig. 5d. When compared with the ^{29}Si NMR of the electrochemically obtained $Li_{15+x}Si_4$ phase (marked with green dotted line),[5] a difference of -127 ppm was observed. This is consistent with the positive shifts observed in ^7Li NMR results due to electron shielding/deshielding phenomena for the respective nuclei—and again, it indicates the insertion of Mg into the Li-Si Zintl phase to form a ternary. The peak at -110 ppm (marked with purple dash line) is due to the native SiO_2 shell in the silicon starting material. There is an expected and large amount of resonance overlap in Fig. 5c and Fig. 5d spectra due to the complexity of the SEI and decomposition products as well as active materials and it will be the focus of a future study. Overall, the characterization results clearly show the incorporation of small concentrations of Mg in Li-Si chemistry to form ternary Li-M-Si phases.
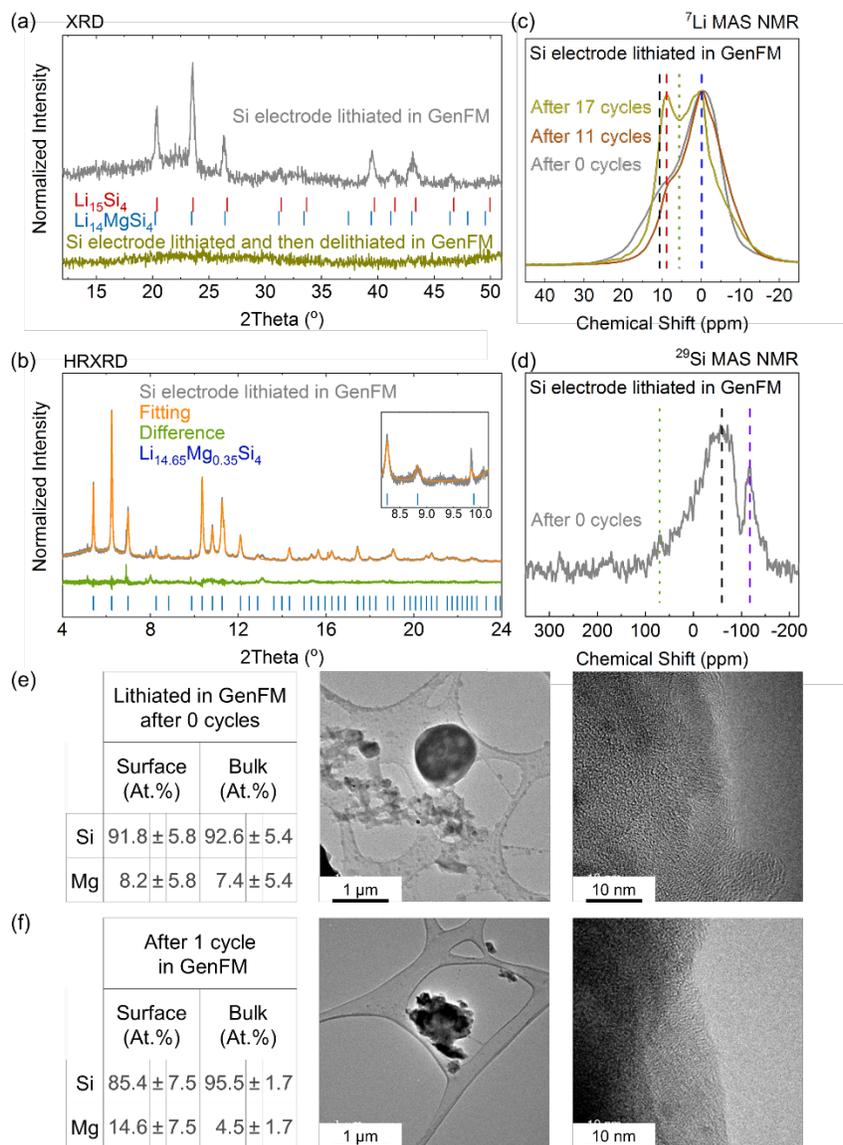
Figure 5. Characterization data of electrochemically treated Si electrodes, lithiated down to 0.01 V vs. Li after different number of cycles, and further delithiated back up to 1.5 V vs. Li, all in half-cell setup using GenFM electrolyte. (a) XRD results of Si electrodes lithiated and then delithiated in GenFM electrolyte. (b) HRXRD and refinement results of Si electrodes lithiated in GenFM electrolyte. The inset shows the zoom-in of the spectra around 10°. (c) ^{7}Li MAS NMR of Si electrodes lithiated in GenFM electrolyte after different number of cycles. (d) ^{29}Si MAS NMR of Si electrodes lithiated in GenFM electrolyte after 0 cycle. Blue dashed line marks diamagnetic Li species in SEI. Black and red dashed lines mark the Li resonance peak centers. Purple dashed line marks the SiO_2 species in original Si material. Green dotted line marks the position of electrochemically lithiated $Li_{15+x}Si_4$ phase.[5] Blue dashed line marks diamagnetic Li species in SEI. Black and red dashed lines mark the Li resonance peak centers. Green dotted line marks the position of electrochemically lithiated $Li_{15+x}Si_4$ phase.[5] (e)(f) TEM and EDS results of Si electrodes lithiated and then delithiated in GenFM electrolyte, respectively. The error bars in EDS results represent the standard deviation of nine different particles.

Conclusions

In this study, we show Li-Mg-Si ternaries to be chemically stable against common electrolyte solvents and that they can be formed *in-situ* through electrochemical co-insertion after adding $Mg(TFSI)_2$ as the secondary salts into the electrolyte formulation in low concentrations. Li-Mg mixed salts stabilize the lithiated Si phases and reduce their side reactions with the electrolytes. The half-cell electrochemical test results show higher capacities, superior cyclabilities, and improved Coulombic efficiencies with the new silicon electrolyte formulations containing $Mg(TFSI)_2$ as the secondary salts to $LiPF_6$ in comparison to the standard electrolyte. The post-electrochemistry NMR, HRXRD, TEM, and EDS characterizations demonstrate that adding Mg secondary salt promotes the doping of small concentrations up to 0.09 Mg per Si into silicon in the bulk during the lithiation process to form relatively more stable amorphous or semicrystalline Li-Mg-Si ternaries; this fundamentally changes the traditional Li-Si binary chemistry while minimally affecting the electrochemical profiles, capacities, and rate capabilities. The results suggest that a rich Zintl chemistry must be further explored fundamentally with this approach where other cations—particularly the multivalents that can form Li-M-Si Zintl phases with minimum activity in the cell otherwise—can be incorporated via the electrolyte to provide *in-situ* stabilization via the formation of Li-M-Si ternaries, Li-M-M'-Si quaternaries, or higher. The applications of the approach in full cells with various M are reported separately in Silicon Deep Dive.

References

1. Baran, V.; van Wüllen, L.; Fässler, T. F., Substitution of Lithium for Magnesium, Zinc, and Aluminum in $Li_{15}Si_4$: Crystal Structures, Thermodynamic Properties, as well as 6Li and 7Li NMR Spectroscopy of $Li_{15}Si_4$ and $Li_{15-x}M_xSi_4$ (M=Mg, Zn, and Al). *Chemistry – A European Journal* **2016,** *22* (19), 6598–6609.
2. Zeilinger, M.; Baran, V.; van Wüllen, L.; Häussermann, U.; Fässler, T. F., Stabilizing the Phase $Li_{15}Si_4$ through Lithium–Aluminum Substitution in $Li_{15-x}Al_xSi_4$ (0.4 < x < 0.8)—Single Crystal X-ray Structure Determination of $Li_{15}Si_4$ and $Li_{14.37}Al_{0.63}Si_4$. *Chemistry of Materials* **2013,** *25* (20), 4113–4121.
3. Antartis, D.; Dillon, S.; Chasiotis, I., Effect of Porosity on Electrochemical and Mechanical Properties of Composite Li-Ion Anodes. *Journal of Composite Materials* **2015,** *49* (15), 1849–1862.
4. Trill, J.-H.; Tao, C.; Winter, M.; Passerini, S.; Eckert, H., NMR Investigations on the Lithiation and Delithiation of Nanosilicon-Based Anodes for Li-Ion Batteries. *Journal of Solid State Electrochemistry* **2011,** *15* (2), 349–356.
5. Key, B.; Bhattacharyya, R.; Morcrette, M.; Seznec, V.; Tarascon, J. M.; Grey, C. P., Real-Time NMR Investigations of Structural Changes in Silicon Electrodes for Lithium-Ion Batteries. *Journal of the American Chemical Society* **2009,** *131* (26), 9239–9249.
6. Key, B.; Morcrette, M.; Tarascon, J. M.; Grey, C. P., Pair Distribution Function Analysis and Solid State NMR Studies of Silicon Electrodes for Lithium Ion Batteries: Understanding the (De)lithiation Mechanisms. *Journal of the American Chemical Society* **2011,** *133* (3), 503–512.
7. Nesper, R.; Curda, J.; Von Schnering, H. G., Li_8MgSi_6, a novel Zintl Compound Containing Quasi-Aromatic Si_5 Rings. *Journal of Solid State Chemistry* **1986,** *62* (2), 199–206.
8. Herbst, J. F.; Meyer, M. S., Structural, Electronic, and Hydriding Properties of Li_2MgSi. *Journal of Alloys and Compounds* **2010,** *492* (1), 65–68.
9. Michan, A. L.; Leskes, M.; Grey, C. P., Voltage Dependent Solid Electrolyte Interphase Formation in Silicon Electrodes: Monitoring the Formation of Organic Decomposition Products. *Chemistry of Materials* **2016,** *28* (1), 385–398.
10. Kim, H.; Choi, J.; Sohn, H. J.; Kang, T., The Insertion Mechanism of Lithium into Mg_2Si Anode Material for Li-Ion Batteries. **1999,** *146* (12), 4401–4405.
11. Obrovac, M. N.; Chevrier, V. L., Alloy Negative Electrodes for Li-Ion Batteries. *Chemical Reviews* **2014,** *114* (23), 11444–11502.
12. Wang, H.; Senguttuvan, P.; Proffit, D. L.; Pan, B.; Liao, C.; Burrell, A. K.; Vaughey, J. T.; Key, B., Formation of MgO during Chemical Magnesiation of Mg-Ion Battery Materials. **2015,** *4* (8), A90–A93.

13. Zhang, L.; Liu, Y.; Key, B.; Trask, S. E.; Yang, Z.; Lu, W., Silicon Nanoparticles: Stability in Aqueous Slurries and the Optimization of the Oxide Layer Thickness for Optimal Electrochemical Performance. *ACS Applied Materials & Interfaces* **2017,** *9* (38), 32727–32736.

Part 3. The Soluble Species

Stability of Glyme-Based Electrolytes for Model Silicon Electrodes: Effect on Corrosion and Passivation

Guang Yang (ORNL), Gabriel Veith (ORNL), and Jagjit Nanda (ORNL)

Background

Intensive study on the passivation layer (i.e., solid-electrolyte interphase, SEI) formed on the silicon anode has demonstrated that the carbonate-based electrolytes cannot effectively generate a stable SEI upon lithiation/delithiation of the Si anode. Such a statement seems to be applicable to both the model amorphous Si (a-Si) films as well as composite slurry electrodes. The application of the ether-based electrolytes to Si-based lithium-ion battery, to our knowledge, has not been explored to a great extent. The use of ether-based electrolytes is inspired by the fact that the dominant organic SEI components in silicon anodes include diethyl alkyl carbonates, carboxylates, and polymeric ether. The polymeric ether species is expected to possess a certain degree of elasticity, so we hypothesize that the polymeric ether components in SEI would better accommodate the volumetric change of the Si upon lithiation/delithiation, thus leading to a more stable SEI layer. Initial studies in Q2 reflect that the onsite reduction potential of a few ether-based electrolytes, including $LiPF_6$-DME and LiTFSI-DME, was higher than that of the GenII electrolyte. In Q3, we extend such a study on more ether-based electrolytes, including lithium bis (fluorosulfonyl) imide (LiFSI)-DME and the LiFSI-DME-1,1,2,2-tetrafluoroethyl-2,2,3,3-tetrafluoropropyl ether (TTE) system. TTE is a type of fluoroether that can stabilize lithium-sulfur (Li-S)[1] and Li-metal batteries.[2] Here, a 50-nm a-Si thin film was used as the model anode.

Results
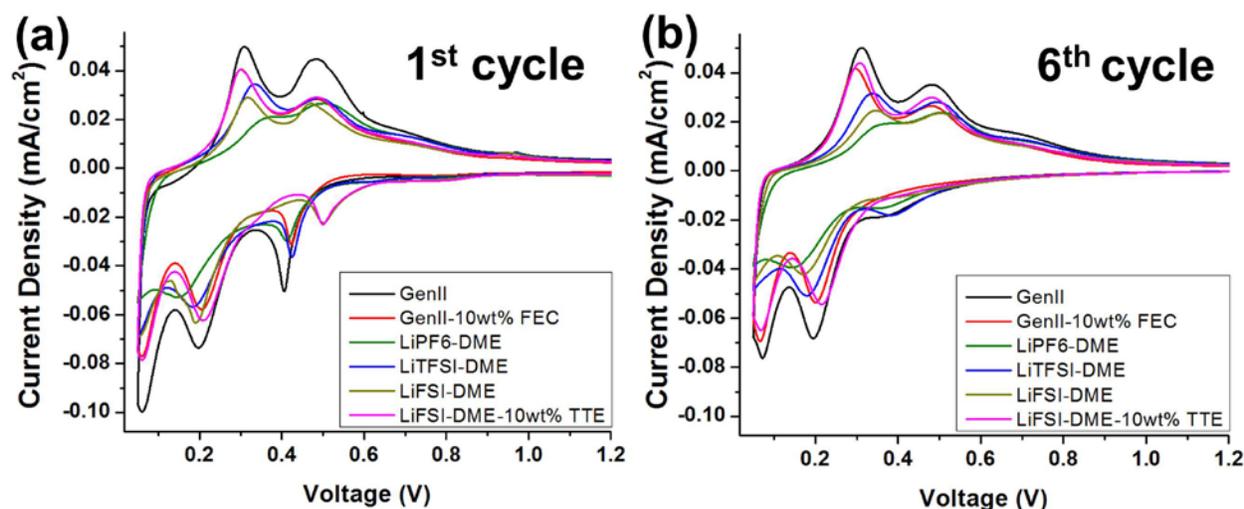
Figure 1. Cyclic voltammograms of a-Si thin-film anodes at the (a) first and (b) sixth cycle with various electrolytes.

We first explored the cyclic voltammetry (CV) of the a-Si anode against a lithium counter electrode using different electrolytes at 0.1 mV/s. The most noticeable difference occurred in the 1st cycle CV profiles of all electrolytes between 0.4 V and 0.6 V. The reduction potential occurred at 0.4 V for the GenII electrolyte, lower than all the other electrolytes. After adding 10 wt% FEC, the reduction potential increased by 0.02 V. The comparable increment occurred to $LiPF_6$-DME and LiTFSI-DME

45

electrolytes. Such a peak occurred at an even higher potential of 0.5 V for the LiTFSI-DME system, regardless of the application of the TTE additive. The higher reduction potential for the LiFSI-DME system indicates greater ease of the electrolyte reduction on the Si surface and/or the irreversible a-Si structural change.[3] This peak became less significant in subsequent CV scans, as shown in Fig. 1b. The parasitic current is notably smaller for GenII-10wt% FEC and LiFSI-DME-10wt% TTE in comparison with other electrolytes at around this voltage. Therefore, we assume that a denser or more stable SEI was formed on the a-Si surface for GenII-10wt% FEC and LiFSI-DME-10wt% TTE electrolytes.

Figure 2. Summary of the parasitic current density during the galvanostatic cycling (GC) – chrono-amperometry (CA) test for a-Si in various electrolytes. During the formation cycle, the a-Si was discharged to 50 mV from OCV. Then, the a-Si anode was cycled between 1.5 V and 50 mV galvanostatically. In between each charge-discharge cycle, a 24-hour potential holding (at 50 mV) CA stage was inserted and the equilibrium current at the end of this stage was recorded. The galvanostatic current was set at 1C-rate (41.7 µA/cm2).

We further use galvanostatic cycling (GC) – chrono-amperometry (CA) test to evaluate the SEI passivation efficiency on the a-Si anode using different electrolytes. Such a test protocol has been described in the Q2 report and elaborated in the caption of Fig. 2. The equilibrium current at the stage is believed to stem from the continuous parasitic reaction of the electrolyte with the lithiated a-Si anode. From Fig. 2, the equilibrium current density decreases upon cycling, extending for many electrolytes. This indicates a better SEI coverage on the surface of the a-Si. Surprisingly, in the initial GC-CA cycle, GenII-10wt% FEC has more than twice the parasitic current than other electrolytes. In the final cycle, the parasitic current of GenII-10wt% FEC experienced a sharp drop during the first 3 cycles and became the smallest among all other electrolytes. This clearly indicates that the SEI formed on the a-Si anode in the first 3 cycles with GenII-10wt% FEC electrolyte is not stable. The change in parasitic current during the first 5 cycles of LiFSI-DME-10wt% TTE is not as abrupt as GenII-10wt% FEC, indicating a more stable SEI formation for the first few cycles. We note here that the SEI formed at the early stage may deform or dissolve into the electrolyte upon long-term galvanostatic cycling. We are exploring the corrosion on the a-Si anode with various electrolytes affected by long-term cycling.

Fig. 3. IR spectra of the a-Si anodes after 5 GC-CA cycles in various electrolytes.

To further explore the surface chemistry of the a-Si after the GC-CA cycling, we measured the infrared (IR) spectra of each sample, as shown in Fig. 3. The most prominent difference of the IR spectra of various a-Si samples is between 800 cm^{-1} and 900 cm^{-1}. An IR peak of high intensity occurs at 838 cm^{-1} for GenII a-Si, indicative of Li_2CO_3 and lithium ethylene dicarbonate

(LEDC). This agrees with our recent work using tip-enhanced Raman spectroscopy on similar a-Si samples.[4] For the rest of the a-Si samples cycled in ether carbonate electrolyte with FEC additive and the ether-based electrolytes, the peak centered at 870 cm^{-1} is due to the breathing mode stemming from the coordination of the alkali metal ions with the ether oxygen.[5] Also, considering other vibrational features of PEO-like species shown in two different frequency regions (in blue font in Fig. 3), it is highly likely that the surface SEI was enriched in PEO for all ether-based electrolytes used here.

Future plan of the research includes consolidating the surface chemistry of the a-Si after the short and prolonged galvanostatic cycling test using IR, XPS and EDX. Unravelling the SEI formation mechanism in different electrolytes is another future focus. NMR will be used to elucidate the SEI dissolution in different electrolytes.

Conclusions

In summary, we explored the passivation and corrosion behavior of various electrolytes on a-Si thin-film anodes. CV profiles indicate that LiFSI-DME-based electrolytes passivate the a-Si better during early-stage electrochemical cycles. GC-CA tests clearly indicate that the SEI formed on a-Si in GenII-FEC electrolyte is metastable for the first 3 cycles. IR spectra of those cycled a-Si anodes indicate that the GenII electrolyte passivation results in Li_2CO_3- and LEDC-rich SEI, whereas the glyme-based electrolytes lead to the formation of the PEO-like SEI on the a-Si surface.

References

1. Azimi, N.; Xue, Z.; Rago, N. D.; Takoudis, C.; Gordin, M. L.; Song, J.; Wang, D.; Zhang, Z., Fluorinated Electrolytes for Li-S Battery: Suppressing the Self-Discharge with an Electrolyte Containing Fluoroether Solvent. *Journal of the Electrochemical Society* **2015,** *162* (1), A64–A68.
2. Ren, X.; Zou, L.; Cao, X.; Engelhard, M. H.; Liu, W.; Burton, S. D.; Lee, H.; Niu, C.; Matthews, B. E.; Zhu, Z., Enabling High-Voltage Lithium Metal Batteries Under Practical Conditions. **2019**.
3. Miao, J.; Thompson, C. V., Kinetic Study of the Initial Lithiation of Amorphous Silicon Thin Film Anodes. *J. Electrochem. Soc.* **2018,** *165* (3), A650–A656.
4. Nanda, J.; Yang, G.; Hou, T.; Voylov, D. N.; Li, X.; Ruther, R. E.; Naguib, M.; Persson, K.; Veith, G. M.; Sokolov, A., Unraveling the Nanoscale Chemical Heterogeneity of Solid Electrolyte Interphase Using Tip-Enhanced Raman Spectroscopy (in press). *Joule* **2019**.
5. Ruther, R.; Yang, G.; Delnick, F. M.; Tang, Z.; Lehmann, M.; Saito, T.; Meng, Y.; Zawodzinski, T. A.; Nanda, J., Mechanically Robust, Sodium-Ion Conducting Membranes for Nonaqueous Redox Flow Batteries. *ACS Energy Letters* **2018**.

Silicon Model Compound – Electrolyte Reaction Studies

N. Sa, S. Cora, J. Vaughey

Background

Recently, we began evaluating the role of adding a soluble Mg salt to the electrolyte to influence the surface layers of the anode as well as the solid-electrolyte interphase (SEI) layer and electrolyte properties. It has been noted from electrochemical quartz-crystal microbalance (EQCM) spectroscopy that the SEI formed in Gen 2 electrolyte was relatively porous (low density) and changed during the charge and discharge cycles. On addition of FEC (a common electrolyte film former added to silicon systems) and cycling, the SEI became more compact and denser. This has been assigned to various attributes of the FEC molecule opening and the role of fluoride incorporation in the film. In this quarter, we continued these studies and have initiated studies evaluating how the Mg salts used also change these electrolyte and reactivity properties.

Results

Major focus in this quarter is to investigate the role of multivalent Mg^{2+} cations when they are added to the conventional Gen2+10%FEC electrolyte. Specifically, we have investigated how Mg^{2+} addition would affect the fundamental electrolyte property of the Gen2+10%FEC electrolyte. Si thin-film anodes made free of binder were used as the anode through all experiments. Among lithium-ion battery silicon researchers, the electrolyte additive fluoroethylene carbonate (FEC) is typically used at 10 wt% in Gen2 (3:7, EC/EMC, 1.2M $LiPF_6$). In the electrolyte, the FEC is thought to undergo a ring-opening reaction with loss of fluoride (to either LiF or an organofluoride compound) to produce a stable conductive film. This film has been found to support fast ionic conductivity of lithium but has a limited lifetime in the system (especially when compared to a vinylcarbonate (VC) -derived film), and its performance degrades once the free monomer is consumed. Previously, we have used EQCM spectroscopy to analyze this film process and noted that the addition of FEC significantly densifies the SEI layer. This quarter, we report on two variables to understand this process: the initial film formation step, and the conductivity of the electrolyte.

We continued with last quarter's efforts to understand the fundamental electrochemical properties of the electrolytes. We have investigated how electrolyte conductivity would be affected by adding the multivalent cation Mg^{2+}. Results in Fig. 1 show a monotonic increase of electrolyte conductivity with addition of a higher volume of FEC additives. For instance, upon adding 20% FEC, we observed a ~50% increase of the conductivity of the electrolyte, Gen2 electrolyte (~11 mS/cm) versus 20%FEC+Gen2 (~14.5 mS/cm). This experimental finding is opposite to what we expected—given that FEC is a co-solvent and adding FEC in theory means to dilute the 1.2 M $LiPF_6$ concentration, which consequently would decrease the conductivity. An increase of the electrolyte conductivity observed here must be ascribed to the change of solvation energy of the $LiPF_6$ salt, and we believe this should be explored in the future.

We evaluated the effect of introducing 0.2 M of $Mg(TFSI)_2$ to the Gen2+10% FEC electrolyte. Measurements confirmed that the addition reduced the electrolyte conductivity. We observed the conductivity of a Gen2+10%FEC electrolyte decreased from 13.5 mS/cm to 1.8 mS/cm upon salt addition. This is consistent with complex cation formation seen in related multivalent electrolytes where complex clusters are formed. In practice, these complex salts would be prevalent during formation cycling and assist in bringing the Mg cation to the active surface, where it would gradually be removed from the electrolyte solution. In theory, we expect an increase of the electrolyte conductivity upon introducing more salt into liquid because it introduces more charge carriers. However, formation of a tighter bond solvation structure could definitely play a role in changing the electrolyte conductivity. More exploration is needed to gain a better understanding of the cause of such a difference.
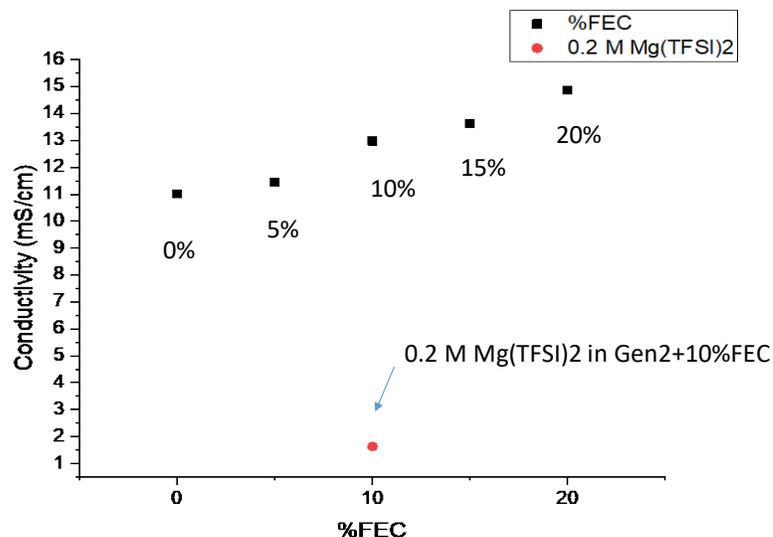
Figure 1. Electrolyte conductivity of the effect of % FEC in GEN2 electrolyte. Square black dot represents electrolyte conductivity of Gen2 with 0%, 5%, 10%, 15%, 20% of FEC. Red dot represents conductivity of introducing a 0.2 M magnesium-bis-(trifluoromethyl-sulfonyl)imide Mg(TFSI)$_2$ salt into the Gen2+10%FEC electrolyte.

Conclusions

We have been investigating the electrolyte properties of the new Mg-containing electrolytes that contain FEC. Specifically, we have shown that adding FEC to the standard Gen2 electrolyte increases the ionic conductivity whereas adding the Mg(TFSI)$_2$ salt initially shows a drop in the measured ionic conductivity. We speculate that this is due to complex cation formation that may or may not involve the FEC solvent. Attempts to date at crystal growth have not yielded crystals of sufficient quality, but studies of the stable solution species are underway.

Silicon Electrolyte Interface Stabilization (SEISta)

S. Jurng, I. Hasa, P. Ross, R. Kostecki (LBNL)

Background

The primary objective of our effort is to clarify and understand the processes occurring at the silicon/electrolyte interface. The reductive decomposition of the electrolyte in lithium-ion systems employing silicon anodes is inevitable because the working potential of the electrode is far below the electrochemical stability window of the electrolyte components. In principle, the insoluble decomposition products precipitating on the electrode surface result in the formation of a passivating surface film that suppresses further electrolyte decomposition.[1,2] However, the inherent instability of the silicon/electrolyte interface strongly inhibits the surface passivation, which is further endangered by the mechanical instability of the electrodes; also, upon alloying with lithium, the electrodes experience a huge volume expansion responsible for active material cracking and consequent instability of the passivating film.[3] A better understanding of the kinetic processes occurring upon cycling will enable efficient implementing of silicon-based electrodes in high-performance lithium-ion batteries. To accomplish this, we address the inherent non-passivating behavior of silicon model electrodes in organic electrolytes. In particular, this last quarter, we have focused on the "Corrosion Task" of the SEISta project, which is a coordinated research thrust aiming to understand and evaluate the non-passivating behavior of silicon anodes. The overall goal of this effort is to provide a basic understanding and ways of effective mitigation of Si anode corrosion in organic carbonate-based electrolytes. Oak Ridge National Laboratory fabricated all the model electrodes for the Corrosion task, and the team at Lawrence Berkeley National Laboratory electrochemically investigated the corrosion currents involved upon cycling.

Results

In the last quarter, our research efforts have been dedicated primarily on evaluating the passivating properties of silicon anodes. A screening study toward defining the best model electrode to be investigated led to selecting silicon thin films (500-nm Si on copper) with a native oxide layer of about 3 nm. We developed electrochemical protocols to use to determine the corrosion currents in a silicon half-cell configuration. Further, we investigated the corrosion behavior of silicon electrodes in the full-cell configuration, in addition to the half-cell configuration, by using $LiFePO_4$ (LFP) as the cathode electrode. LFP acts as the source of a limited amount of lithium and enables a direct visualization of the effect of the silicon corrosion and lithium consumption upon cycling.

The 500-nm Si thin film has been investigated in three electrolyte solutions: 1.2 M $LiPF_6$ EC:EMC (3:7 wt%), 1.2 M $LiPF_6$ EC:EMC (3:7 wt%) + 10%wt. FEC, and 1.2 M LiTFSI EC:EMC (3:7 wt%). Figure 1 reports the galvanostatic cycling test (with associated potentiostatic steps) and the I vs t curves obtained during the constant voltage step at 0.05 V for the 500-nm Si thin film in three different electrolytes. The analysis has been performed by applying the protocol developed within the corrosion task (GCPL + CA).

The $LiPF_6$-based electrolyte presents the largest reductive current density, and the presence of FEC and the substitution of $LiPF_6$ with LiTFSI strongly reduce the current involved in the process. Protocol 1 (GCPL + CA) has been applied to the above-mentioned system to understand and evaluate the effect of different salts ($LiPF_6$ vs LiTFSI) and the effect of effect of the addition of 10%wt. FEC on the passivating properties of silicon.

Interestingly, the residual current detected after 24 hours at 0.05 V is very large for the 1.2 M $LiPF_6$ EC:EMC (3:7 wt%) electrolyte, whereas by substituting $LiPF_6$ with LiTFSI, the current value is about 7 times smaller. The same effect is observed with the addition of 10%wt FEC to the bare 1.2 M $LiPF_6$ EC:EMC (3:7 wt%) solution. Also, the passivation of silicon improves upon cycling, as demonstrated by the lower current values observed after the third potentiostatic step when compared to the first step.
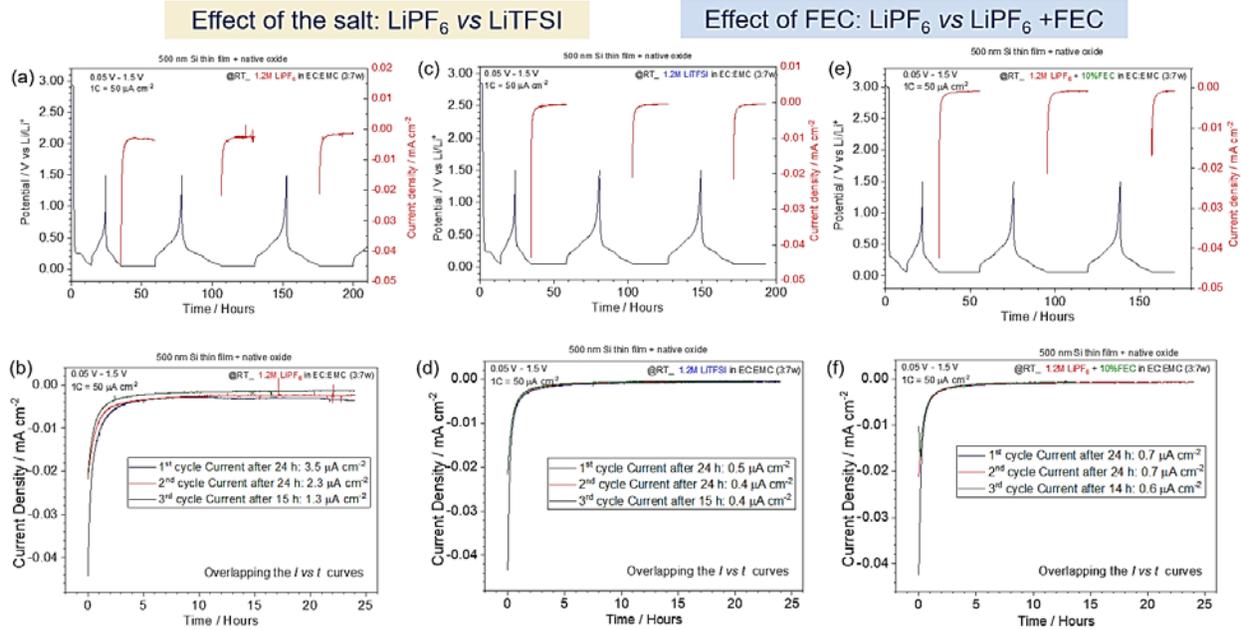
Figure 1. Application of Protocol 1 (GCPL + CA) to the 500-nm Si thin-film model electrode by using (a, b) 1.2 M LiPF$_6$ EC:EMC (3:7 wt%), (c, d) 1.2 M LiPF$_6$ EC:EMC (3:7 wt%) + 10%wt. FEC, and (e, f) 1.2 M LiTFSI EC:EMC (3:7 wt%). (a, b, c) show the galvanostatic cycling with associated potentiostatic step at 0.05 V. (b, d, f) reports the related current density measurement during the potentiostatic step.

Figures 2 shows the voltage profiles and Fig. 3 shows the cycling performance of LFP/Si cells using three different electrolyte solutions: 1.2 M LiPF$_6$ EC:EMC (3:7 wt%), 1.2 M LiPF$_6$ EC:EMC (3:7 wt%) + 10%wt. FEC, and 1.2 M LiTFSI EC:EMC (3:7 wt%).
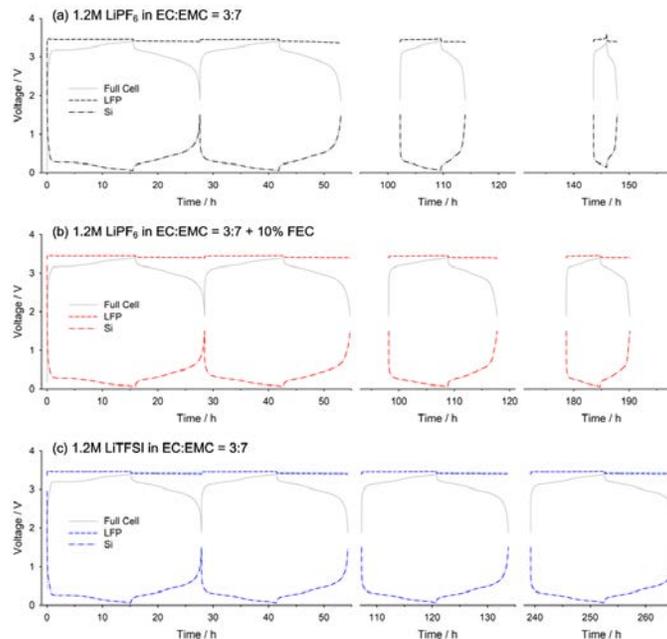
Figure 2. The voltage profiles of LiFePO$_4$/Si cells containing the 500-nm Si thin-film model electrodes (1st, 2nd, 5th, and 10th cycle) with (a) 1.2 M LiPF$_6$ EC:EMC (3:7 wt%), (b) 1.2 M LiPF$_6$ EC:EMC (3:7 wt%) + 10%wt FEC, and (c) 1.2 M LiTFSI EC:EMC (3:7 wt%).
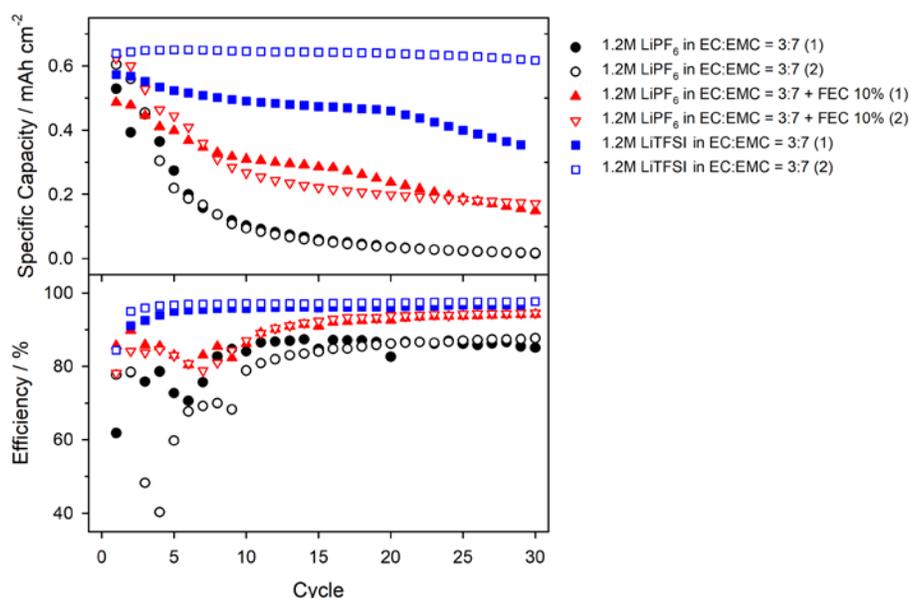
Figure 3. Cycling performance and efficiency of LiFePO4/Si cells containing the 500-nm Si thin-film model electrodes with different electrolyte solutions.

As mentioned above, this full-cell system has a very limited amount of lithium, such that lithium loss upon cycling is directly visible from the remaining capacity of LFP/Si cells. In the initial 10 cycles, the cell with 1.2 M LiPF$_6$ EC:EMC (3:7 wt%) solution lost almost 80% of its initial capacity, which indicates that the lithium consumption from the corrosion behavior on the silicon surface had been very severe. The presence of FEC and the substitution of LiPF$_6$ with LiTFSI improved the cycling performance significantly, comparable to the previous results with the half cells. It should be noted that the cell with 1.2 M LiTFSI EC:EMC (3:7 wt%) presents remarkably good cycling performance and only loses a marginal amount of lithium upon cycling. These results suggest that the corrosion behavior on silicon affects the performance of full cells such that it needs to be reduced for the commercialization of silicon.

To calculate the amount of consumed lithium from two possible sources—electrolyte decomposition and lithium trapping—we adopted a calculation model.[4] In this calculation model, the irreversible capacity originating from electrolyte decomposition is the difference between the consumed lithium during each lithiation step and the actual amount of inserted lithium to silicon in this step. The irreversible capacity originating from lithium trapping can be obtained by subtracting the delithiation capacity from the lithiation capacity in that cycle. The amount of inserted lithium (lithiation capacity) can be accessed by the quasi-open-circuit voltage (QOCV) at the end of each lithiation step. Figure 4 presents the schematic of the approach to the SOC value of each cycle through the QOCV and the galvanostatic intermittent titration technique (GITT) profile.
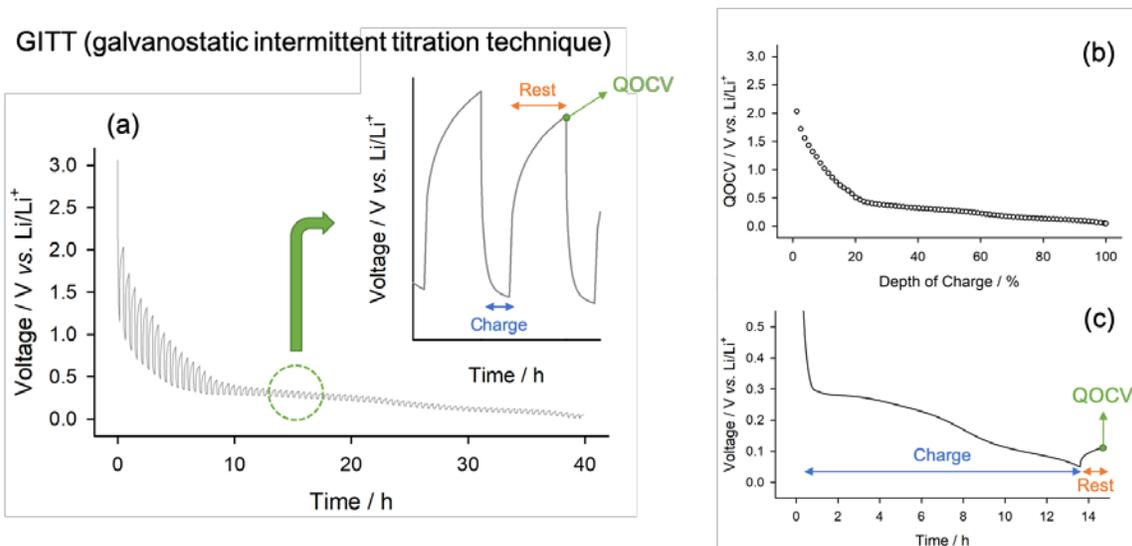
Figure 4. Schematic of the procedure to estimate the actual state of charge (SOC) of silicon electrodes. From (a) the GITT profile, the (b) relation between quasi-open-circuit voltage (QOCV) and SOC is obtained. At the end of each lithiation step, the SOC is extrapolated from (c) the observed QOCV in relation to the QOCV value on the GITT profile.

Figure 5 shows the calculated irreversible capacity (capacity loss) originating from electrolyte decomposition and lithium trapping in $LiFePO_4$/Si full cells. Overall, electrolyte decomposition is dominant over lithium trapping regardless of electrolytes. It is noteworthy that the cell with 1.2 M $LiPF_6$ EC:EMC (3:7 wt%) solution loses the most lithium over the early 10 cycles, but also, that it shows surface instability (trapped lithium <0). Again, this suggests the non-passivating behavior of silicon anodes in the standard condition. The calculated irreversible capacity from electrolyte decomposition correlates well with the cycling performance of full cells, indicating that electrolyte decomposition is the main reason of cycling decay of $LiFePO_4$/Si cells.

| Sum of electrolyte decomposition | **0.95** mAh/cm^2 |
| Sum of trapped lithium | 0.03 mAh/cm^2 |

| Sum of electrolyte decomposition | 0.54 mAh/cm^2 |
| Sum of trapped lithium | **0.15** mAh/cm^2 |

| Sum of electrolyte decomposition | 0.30 mAh/cm^2 |
| Sum of trapped lithium | 0.08 mAh/cm^2 |
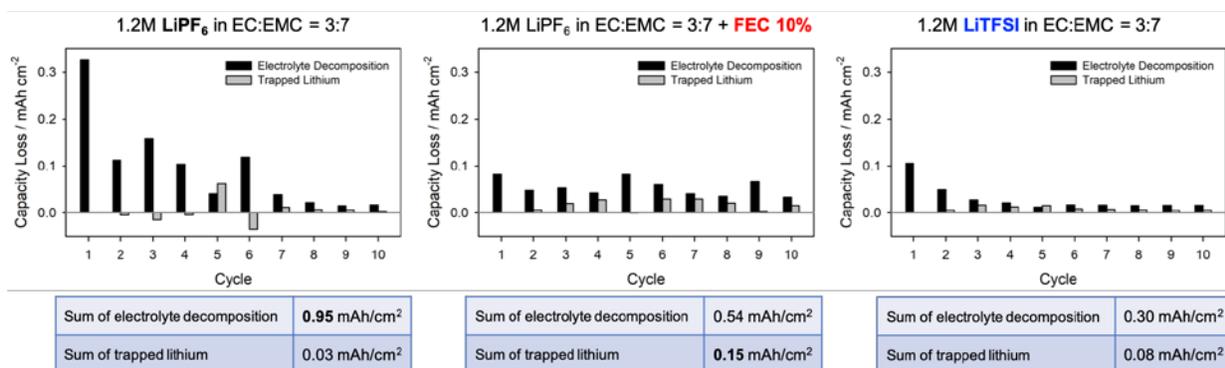
Figure 5. The calculated capacity loss from electrolyte decomposition and lithium trapping in $LiFePO_4$/Si cells containing the 500-nm Si thin-film model electrodes with different electrolyte solutions.

Conclusions

In summary, the non-passivating behavior of silicon thin films has been observed directly for the first time as an independent effect from the cracking of silicon particles due to lithiation. A visualization of the improved passivation properties upon cycling has been quantified, suggesting a thickening of the passivating film on the silicon surface. The beneficial effect of FEC for SEI stability has been confirmed in both half- and full-cell configurations. Additionally, the use of LiTFSI as an alternative salt to improve the SEI stability is proposed.

We also investigated the effect of corrosion of silicon in the full-cell configuration using LFP/Si cells. Due to the non-passivating nature of silicon thin films, the lithium consumption upon cycling was substantial for the standard electrolyte solution. The full-cell results are comparable to our previous observation with the half-cells such that the use of FEC and LiTFSI mitigates such silicon corrosion. Further, the calculation model concludes again that the electrolyte decomposition and surface instability on the silicon anode is the main reason for the irreversible capacity and capacity loss of LFP/Si cells.

References

1. E. Peled, *J. Electrochem. Soc.*, **126**, 2047–2051 (1979).
2. M. Winter, *Zeitschrift für Phys. Chemie.*, **223**, 1395–1406 (2009).
3. M.N. Obrovac, V.L. Chevrier, *Chem. Rev.*, **114**, 11444–11502 (2014).
4. J. G. Lee, *J. Electrochem. Soc.*, **162**, A1579–A1584 (2015).